Astronomy & Astrophysics manuscript no. output
November 12, 2026
©ESO 2026

Euclid: Data Release 1 (DR1) – Bayesian 3D shape inference of star-forming galaxy populations★

M. Dunn, M. Huertas-Company, J. H. Knapen, V. Pandya, H. Zhang, L. Quilley, A. van der Wel, E. Duran-Camacho, et al.

(Full author list and affiliations details can be found after the references)

November 12, 2026

ABSTRACT

Understanding the intrinsic three-dimensional (3D) shapes of galaxies provides crucial insights into their formation and evolution, but determining these from two-dimensional (2D) projected observations remains challenging. We apply a Bayesian inference framework to optical imaging of galaxies in the Euclid Data Release 1, leveraging its larger sample sizes to test the scalability and robustness of this methodology. Applying Hamiltonian Monte Carlo (HMC) sampling to Sérsic axis ratios and effective radii, we constrain the population-level mean intrinsic 3D ellipticity, triaxiality, and size, together with their covariances. This analysis is performed for 40 864 304 star-forming galaxies with stellar masses $M_* = 10^9$–$10^{10.5} M_\odot$ at redshifts $0 < z < 1.2$. Our sample size exceeds previous shape inference studies by factors of 440–52 800 relative to early observations by the *James Webb* Space Telescope (JWST), and factors of 440–17 600 relative to legacy observations from the *Hubble* Space Telescope (HST) in overlapping stellar mass-redshift bins, enabling substantially finer binning alongside improved statistical constraints on shape evolution. We additionally include over 9 million galaxies at $z < 0.5$, a regime historically limited by sample size in previous shape inference studies. We recover key evolutionary trends identified in previous smaller-sample studies. We find high mean ellipticities at the population level ($\mu_E \sim 0.600$–0.821) across all bins, indicating that the underlying 3D shape distributions are statistically dominated by flattened, non-spherical geometries. Most notably, we recover the decline of the prolate fraction towards the present day at low masses ($M_* = 10^9$–$10^{9.5} M_\odot$) reported by previous studies. This trend is seen consistently in comparable analyses of independent data sets spanning different depths and resolution regimes, showing that it is not an artefact of small-sample statistics, suggesting it may be a genuine feature of galaxy evolution. We also identify future methodological improvements for subsequent *Euclid* data releases.

Key words. Galaxies: evolution – Galaxies: statistics – Galaxies: structure – Methods: statistical – Methods: data analysis

1. Introduction

The study of galaxy 3D geometries through projected shapes spans nearly a century, and remains crucial to understanding how the diverse morphologies seen today formed and evolved. Such studies assume that galaxies can be approximated as 3D ellipsoids classified by their degree of flattening in certain directions. Hubble (1926) demonstrated that nearby galaxies have projected ellipticities too round to be explained by randomly orientated disc galaxies alone, leading to his well-known classification system, and the introduction of the flattened 'lenticular' galaxy class (de Vaucouleurs 1959; Sandage 1961). Subsequent analyses incorporated projected axis ratios for late- and early-type galaxies (e.g., Sandage et al. 1970; Binney 1978; Noerdlinger 1979). This eventually led to more 'triaxial' models to explain the kinematics of nearby elliptical galaxies (e.g., Contopoulos 1956; Stark 1977; Binney 1978).

Modern imaging has enabled statistical inference of intrinsic 3D galaxy shapes from projected measurements, revealing several robust trends in the local Universe (e.g., Lambas et al. 1992; Alam & Ryden 2002; Ryden 2004; Vincent & Ryden 2005; Méndez-Abreu et al. 2010; Costantin et al. 2018). In particular: intrinsic roundness increases with luminosity and stellar mass (Padilla & Strauss 2008; Rodríguez & Padilla 2013); spiral discs are thicker and less circular than previously assumed, with thickness increasing with luminosity (Rodríguez & Padilla 2013); massive elliptical galaxies are more spherical than their low-mass counterparts, as confirmed by stellar kinematics (e.g., Binney 1985; Franx et al. 1991; Ryden 1992; Tremblay & Merritt 1995; Emsellem et al. 2011; Cappellari 2016); and local dwarf galaxies span a wide range of morphologies, including both discs and spheroids (e.g., Caldwell 1983; Ichikawa et al. 1986; Ferguson & Sandage 1989; Ferguson & Binggeli 1994; Sánchez-Janssen et al. 2010; Kado-Fong et al. 2021).

Hubble Space Telescope (HST) observations allowed the extension of intrinsic shape studies to massive galaxies at higher redshifts, showing that discs and spheroids are typically more compact and thick than at low redshift (e.g., Elmegreen et al. 2004a,b; van der Wel et al. 2014b; Zhang et al. 2022; Hamilton-Campos et al. 2023). Using projected axis ratios, Chang et al. (2013) found that massive quiescent galaxies, $\log_{10}(M_*/M_\odot) = 9.0$–$11.0$, at $1.0 < z < 2.5$ from the Cosmic Assembly Near-infrared Deep Extragalactic Legacy Survey (CANDELS; Grogin et al. 2011; Koekemoer et al. 2011) are more disc-like at high redshift (before mergers destroyed those discs), whereas lower-mass galaxies become increasingly disc-dominated towards $z = 0$. Similarly, van der Wel et al. (2014a, hereafter vdW14a) showed that star-forming galaxies with $M_* > 10^{10} M_\odot$ remain disc-dominated up to $z \sim 2$, whereas lower-mass galaxies exhibit rising fractions of elongated (prolate) shapes at higher redshifts, consistent with other observational studies (e.g., Cowie et al. 1995; Ravindranath et al. 2006; Law et al. 2012; Yuma et al. 2012). Incorporating both projected sizes and axis ratios, Zhang et al. (2019, hereafter Z19) further confirmed a transition from

★ This paper is published on behalf of the Euclid Consortium.

predominantly elongated (prolate) populations at high redshift to disc-dominated systems at later times. Hoffmann et al. (2022) found minimal evolution in disc properties in the Cosmological Evolution Survey (COSMOS; Scoville et al. 2007) galaxies, suggesting that most present-day discs formed early and evolved largely undisturbed.

Recently, Pandya et al. (2024, hereafter P24) demonstrated the power of differentiable Bayesian modelling with Hamiltonian Monte Carlo (HMC) sampling to constrain intrinsic 3D shapes from *James Webb* Space Telescope (JWST) Cosmic Evolution Early Release Science (CEERS; Finkelstein et al. 2023) observations of star-forming galaxies with $\log_{10}(M_*/M_\odot) = 9.0$–$10.5$ at $0.5 < z < 8$, successfully reproducing earlier HST-CANDELS results at dramatically reduced computational cost. They confirmed the evolutionary trend identified in previous work in which elongated geometries dominate low-mass galaxies ($M_* = 10^9$–$10^{9.5} M_\odot$) at high redshift, declining from around 50–80% at $3 < z < 8$ to 25% at $0.5 < z < 1.0$. Their analysis further revealed a transition from triaxial (oval) to increasingly axisymmetric (circular) disc configurations over time.

The HST-CANDELS and JWST-CEERS studies firmly establish the prolate-to-disc evolutionary trend, but are limited by relatively small samples – often only a few hundred galaxies per mass-redshift bin. Large-scale surveys such as *Euclid* (Euclid Collaboration: Mellier et al. 2025) provide an opportunity to test the robustness and scalability of the P24 methodology on a far larger sample and in a different observational regime. Aimed at probing the evolution of the dark Universe, *Euclid* is delivering high-quality imaging and spectroscopic data for millions of galaxies across a wide range of redshifts. Both its wide-field and deep-field surveys provide unprecedented statistical power to test whether 3D shape evolution trends persist across the broader galaxy population and explore dependencies on environment and other physical properties.

In this work, we apply the Bayesian inference framework of P24 to optical imaging from Data Release 1 (DR1; Euclid Data Release 1 2026; Euclid Collaboration: Aussel et al., in prep.). We leverage substantially larger samples to statistically infer the 3D shape distributions of star-forming galaxies with stellar masses $\log_{10}(M_*/M_\odot) = 9.0$–$10.5$ at photometric redshifts $0 < z < 1.2$. In Sect. 2, we detail our methods. Section 3 describes the *Euclid* data sample used for this work. In Sect. 4, we present the inferred 3D shape distributions and their evolution with mass and redshift, and visually inspect and examine the properties of galaxies in the sample. We discuss the implications of our findings in Sect. 5 and summarise our conclusions in Sect. 6. We emphasise that the primary goal of this work is to test the scalability and robustness of the P24 inference framework on a vastly larger and observationally distinct sample, by applying the same methodology to DR1. A detailed astrophysical interpretation of the inferred shape distributions, together with efforts to address the methodological and observational limitations identified here – in particular, the move beyond single-band optical imaging and single-Sérsic morphologies – is deferred to a forthcoming paper.

Throughout this paper, we use capital letters (A, B, C) for intrinsic 3D axes, and lowercase letters (a, b) for projected 2D axes. We use $\log_{10}(a)$ and $\log_{10}(A)$ as shorthand for $\log_{10}(a/\mathrm{kpc})$ and $\log_{10}(A/\mathrm{kpc})$, following the convention of Z19 and P24. We assume a flat Lambda cold dark matter (ΛCDM) cosmology with $H_0 = 67.74\,\mathrm{km\,s^{-1}\,Mpc^{-1}}$, $\Omega_\mathrm{m} = 0.3089$, and $\Omega_\Lambda = 0.6911$ (Planck Collaboration et al. 2016). Magnitudes are given in the AB system (Oke 1974).

2. Methodology

In this section, we describe how galaxies are modelled as 3D ellipsoids, how populations of intrinsic shapes are projected onto the observed plane, and the population-level Bayesian inference framework of P24 that we adopt.

As in previous studies (e.g., vdW14a; Z19; P24), we approximate galaxies as triaxial ellipsoids with intrinsic semi-axes $A \geq B \geq C$, parameterised by the length of the semi-major axis A, the ellipticity E, defined as

$$E = 1 - C/A\ , \tag{1}$$

and triaxiality T, defined as

$$T = \frac{A^2 - B^2}{A^2 - C^2}\ . \tag{2}$$

Using these definitions, ellipsoids can be classified into three general geometries: (1) 'spheroidal' ($A \sim B \sim C$ and $E \sim 0$), appearing round from any viewing angle; (2) 'oblate' ($B \sim A$, $E \sim 1$, and $T \to 0$), flattened in one direction, appearing as flat discs when viewed 'edge-on' and round when viewed face-on; or (3) 'prolate' ($B \sim C$, $E \sim 1$, and $T \to 1$), flattened in two directions, appearing as a 'cigar-like' shape when viewed edge-on. There are also intermediate cases where all three axes differ greatly ($0 < T < 1$) known as 'triaxial ellipsoids' or non-axisymmetric discs, appearing as flattened oval discs (P24). Given this, we expect triaxiality T (Eq. 2) to become increasingly ill-constrained as ellipticity E (Eq. 1) approaches zero, since both the numerator and denominator of T vanish for nearly spherical ellipsoids. Figure 5 of P24 illustrates the different projections and cross-sections of these 3D ellipsoids, and how their populations appear projected in 2D space.

We adopt the classification boundaries of figure 1 in Z19 and figure 2 in vdW14a, classifying galaxies by their location in intrinsic 3D axis-ratio space (C/A–B/A), where C/A and B/A are obtained by rearranging Eqs. (1) and (2). The triaxiality parameter T is essential for distinguishing oblate from prolate populations, since both have large ellipticities and similar edge-on appearance. We focus on identifying the dominant intrinsic shape distributions (specifically spheroidal, oblate, or prolate) for galaxy populations in each bin of stellar mass and redshift. Imaging data alone enables us to constrain the intrinsic shape distribution of a population, but it is not enough to recover the intrinsic shapes of individual galaxies in bins where ellipsoid types are ambiguously mixed – such cases would require additional data (e.g., kinematic measurements).

We use the empirical library of Z19 and P24, comprising 1 million 3D ellipsoids spanning a uniform grid in E–T–$\log_{10}(A)$ space, each characterised by an intrinsic shape vector $\boldsymbol{\theta} = (E, T, \log_{10} A)$ and observed from 100 000 simulated viewing angles. Projecting these ellipsoids and marginalising them over all viewing angles (Binney 1985; van de Ven & van der Wel 2021) produces population-level probability distribution maps in projected b/a versus $\log_{10}(a)$, binned on a 20×20 grid. The library further incorporates realistic observational uncertainties: a Rice distribution (Rix & Zaritsky 1995, appendix C) scatters each ellipsoid's projected axis ratio assuming $\Delta(b/a) = 0.04$, the resulting perturbation is propagated into the projected size, and $\log_{10}(a)$ is additionally smeared by a Gaussian of width 0.03 dex (P24, section 3.1).

Following P24, we assume that each ellipsoid's intrinsic shape vector is drawn from a trivariate Gaussian distribution with an unknown mean shape vector $\boldsymbol{\mu} = (\mu_E, \mu_T, \mu_{\log_{10} A})$ and an unknown covariance matrix (P24, equation 4), characterised

by standard deviations σ_E, σ_T, and $\sigma_{\log_{10}(A)}$, and covariance $\rho_{E,\log_{10}(A)}$ between 3D ellipticity and size. Central to this approach is the assumption that, within a given bin of stellar mass and redshift, all galaxies are 2D projections of a single parent 3D shape distribution, described by this one trivariate Gaussian. The inference thus constrains the parameters of that parent distribution rather than classify individual galaxies, whose projected shapes are intrinsically degenerate. We discuss the validity of the single-distribution assumption in Sect. 5.3. These seven population-level parameters constitute the shape parameters we infer for each mass–redshift bin in our sample.

We perform Bayesian parameter estimation following P24 using the `PyMC` probabilistic programming framework (Salvatier et al. 2016) with the No U-Turn Sampler (NUTS; Hoffman & Gelman 2014). We use weakly informative uniform priors for all seven shape parameters, only imposing physical constraints while allowing the posterior distributions to be driven primarily by the observed data. A visualisation of the full Bayesian model used can be found in figure 6 of P24. We evaluate the Poisson likelihood between observed and model 2D b/a–$\log_{10}(a)$ histograms; only cells populated by the observed galaxies above the minimum-size cut (Sect. 3.1) and within $\log_{10}(a) \in [-1, 1]$ are considered, and the model histogram is normalised over these cells. We run four parallel sampling chains, with 5000 tuning and 2000 sampling iterations, and a target acceptance rate of 0.95, for all bins. We assess convergence using standard NUTS diagnostic statistics, such as $\hat{R}$ (Vehtari et al. 2021), effective sample size (ESS; Gelman et al. 2013; Gong & Flegal 2016; Vats et al. 2019), Monte Carlo standard error (MCSE) in the Markov chain Monte Carlo (MCMC; Flegal & Jones 2010, 2011), and Bayesian fraction of missing information (BFMI; Betancourt 2016). Together, these diagnostics assess sampler performance, probing complementary aspects of convergence, sampling efficiency, and goodness-of-fit, providing confidence that the posteriors are both well-sampled and consistent with the observed distributions.

3. Data sample

3.1. DR1 catalogue selection

We use DR1 optical (VIS) imaging (I_E; Euclid Collaboration: Cropper et al. 2025; Euclid Collaboration: McCracken et al., in prep.) from the Euclid Wide Survey (EWS; Euclid Collaboration: Scaramella et al. 2022; Euclid Collaboration: Tereno et al., in prep.), with approximately 1900 deg^2 of sky coverage. More detailed information on DR1, the *Euclid* observing strategy, and VIS processing and data products can be found in Euclid Collaboration: Aussel et al. (in prep.), Euclid Collaboration: Scaramella et al. (2022), Euclid Collaboration: Tereno et al. (in prep.), and Euclid Collaboration: McCracken et al. (in prep.). We construct our parent sample from catalogues built with the MER (Euclid Collaboration: Kümmel et al., in prep.) and PHZ (Euclid Collaboration: Hartley et al., in prep.) processing functions (PFs). Both projected sizes and axis ratios for galaxies come from elliptical 2D Sérsic profile fits (Sérsic 1963) of *Euclid* VIS images using `SourceXtractor++` (`SE++`; Bertin et al. 2020; Kümmel et al. 2022) from MER, as described in Euclid Collaboration: Quilley et al. (2026). These parameters are point spread function (PSF)-corrected through forward-modelling during Sérsic fitting. We define a galaxy's projected size a as its angular Sérsic effective (half-light) semi-major axis (in arcseconds), following the convention of van der Wel et al. (2014b), and projected axis ratio b/a as the Sérsic axis ratio. We use the photometric redshifts, stellar masses, star-formation rates (SFRs), and rest-frame magnitudes from the PHZ PF (Euclid Collaboration: Enia et al., in prep.), adopting the medians of their posterior probability distributions as point estimates. We do not propagate the photometric-redshift uncertainties into the inference directly. When comparing with spectroscopic redshifts, Euclid Collaboration: Enia et al. (in prep.) report an overall $\sigma_{\rm NMAD} \approx 0.021$ and outlier fraction ($f_{\rm out}$) of 3.7% for EWS-like processing of Euclid Deep Field North (EDF-N) for the Northern hemisphere (EWS-N), and $\sigma_{\rm NMAD} \approx 0.027$ and $f_{\rm out} \approx 7.6\%$ for Euclid Deep Field Fornax (EDF-F) for the Southern hemisphere (EWS-S). These degrade to $\sigma_{\rm NMAD} \approx 0.034$–$0.048$ and $f_{\rm out} \approx 9.4$–16.2% near the faint end of our magnitude range at $23 < I_E \leq 25$. This effect on physical sizes is quantified in Sects. 3.1.

After building a magnitude-limited sample from these catalogues, we applied several quality selection cuts recommended in Euclid Collaboration: Quilley et al. (2026) and Euclid Collaboration: Enia et al. (in prep.) to ensure reliable measurements and physical parameters. We also include several of our own selection cuts, such as excluding sources with fractional uncertainties $> 10\%$ in either the Sérsic effective radius or axis ratio values (see Appendix B for a comparison of these uncertainties against independent HST measurements). We also exclude sources with projected sizes smaller than the PSF full width at half-maximum (FWHM) for the VIS filter (0.″16; Euclid Collaboration: Scaramella et al. 2022). Our model can in principle recover smaller intrinsic sizes, but this limit ensures that resolved galaxies dominate the analysis. As in Z19 and P24, this cut primarily affects more massive bins and those at higher redshifts. Lastly, we restrict the analysis to galaxies with stellar masses $M_* = 10^9$–$10^{10.5} M_\odot$ at photometric redshifts $0 < z < 1.2$, and exclude sources with missing or non-finite Sérsic, stellar mass, or redshift values. The full list of these selection cuts is detailed in Appendix A.

3.2. sSFR selection

Although galaxy populations within a given bin of stellar mass and redshift span a range of intrinsic geometries, our methodology models each population as a mixture of predominantly spheroidal, oblate, and prolate shapes. To maximise population homogeneity, we restrict our analysis to star-forming galaxies, since quiescent galaxies not only differ in their 3D shape distributions (Chang et al. 2013), but are harder to detect and grow increasingly rare at higher redshifts (e.g., Pandya et al. 2017). In principle, the same analysis could be applied to purely quiescent populations instead. Following Pandya et al. (2017), we compute the median specific star formation rate (sSFR) of the zero-slope star-forming main sequence (SFMS) in each redshift bin, adopting a large SFMS scatter of 0.45 dex ($1\,\sigma$) for all redshift slices (P24). We then classify galaxies in each redshift bin by their offset below the median SFMS: (1) 'star-forming', offset by less than 0.45 dex ($1\,\sigma$) below the SFMS; (2) 'transition', offset by 0.675–1.575 dex (1.5–3.5 σ) below the SFMS; and (3) 'quiescent', offset by more than 1.575 dex ($3.5\,\sigma$) below the SFMS. This selection is shown in the sSFR–M_* diagrams for each redshift slice in Fig. C.1.

3.3. Colour-based selection

To further mitigate contamination by quiescent galaxies, we also apply a colour-based galaxy classification. Following Pandya et al. (2017, appendix A), we construct a $(U - V)$ versus $(V - J)$

colour diagram (Van Dokkum et al. 2015) for the sSFR-classified sample in each redshift slice, using rest-frame magnitudes and SED-fitting-derived optical dust attenuation A_V from Euclid Collaboration: Enia et al. (in prep.). As shown in Fig. C.2, points are colour-coded by A_V and organised into three columns by the sSFR-based classification described above, with each column containing a 'quiescent wedge' that is defined in Van Dokkum et al. (2015, equation 3) as galaxies that satisfy the relations

$$\begin{aligned}(V-J) &< 1.5,\\ (U-V) &> 1.3,\\ (U-V) &> 0.8\,(V-J)+0.7.\end{aligned} \tag{3}$$

Excluding transition and quiescent galaxies and star-forming galaxies in quiescent wedges, the sample size becomes 104 540 419.

3.4. Final sample

After applying the quality cuts described in Sect. 3.1 to our star-forming sample, the resulting sample size is 70 498 316. Our final sample consists of 40 864 304 star-forming galaxies within the stellar mass range $M_* = 10^9$–$10^{10.5} M_\odot$ at photometric redshifts $0 < z < 1.2$, with a limiting magnitude of $I_E \leq 24.5$. We bin galaxies by $\Delta \log_{10}(M_*/M_\odot) = 0.5$ and $\Delta z = 0.2$. We convert projected sizes a from arcseconds to physical units of kiloparsec in each redshift bin. Photometric-redshift uncertainties propagate into the physical sizes through the angular-diameter distance. We estimate this contribution by redrawing each galaxy's redshift from its 68% credible interval estimated by the PHZ PF and recomputing $\log_{10}(a/\mathrm{kpc})$. The resulting median scatter at all redshift intervals is at or below the 0.03 dex size smearing already included in the model library (Sect. 2), so photometric-redshift uncertainties do not significantly affect the inferred shape parameters. The 2D projected b/a–$\log_{10}(a)$ histograms for $b/a \in [0, 1]$ and $\log_{10}(a) \in [-1, 1]$ (corresponding to $a \sim 0.1$–10 kpc) for each *Euclid* mass-redshift bin are shown in Fig. 1, with the galaxy counts indicated in each panel. These distributions serve as input to our shape inference model.

We adopt a limiting magnitude of $I_E \leq 24.5$ to balance the sample size against reliable Sérsic measurements and completeness. In Appendix B, we assess the reliability of the Sérsic measurements themselves by comparing single-visit EDF-F DR1 measurements at EWS depth against independent HST-based measurements in the Galaxy Evolution from Morphology and SEDs (GEMS; Rix et al. 2004) field (Figs. B.1 and B.2), finding behaviour consistent with the equivalent Q1 comparison of Euclid Collaboration: Quilley et al. (2026). In Appendix E, we assess the detection fraction using single-Sérsic fits with `SourceXtractor++` on mock sources from the *Euclid* Morphology Challenge (Euclid Collaboration: Merlin et al. 2023; Euclid Collaboration: Bretonnière et al. 2023). Morphological completeness remains high across the b/a–size plane for our magnitude-limited sample, including for large face-on discs that are most vulnerable to surface-brightness biases (Fig. E.1). We also assess the stellar mass completeness of our magnitude-limited sample. Future *Euclid* data releases are expected to improve mass completeness through a larger sample size, allow wider mass and redshift ranges, and allow finer binning.

4. Results

In this section, we present constraints on the 3D shapes of DR1 star-forming galaxies with $M_* = 10^9$–$10^{10.5} M_\odot$ at $0 < z < 1.2$. Table F.2 summarises the inference results for each mass-redshift bin based on random draws from the posterior. The convergence diagnostic statistics for each bin can be found in Table F.1. Across all mass-redshift bins, we find $\hat{R} < 1.01$ for all sampling chains, no divergent transitions, no low BFMI values, and sufficiently large effective sample sizes, together indicating good convergence and fit (Vehtari et al. 2021; Betancourt 2016). The observed and posterior-mean model histograms, along with their residuals, are provided for each bin in Appendix H.

We examine the evolution of inferred 3D ellipticity (Sect. 4.1), triaxiality (Sect. 4.2), and size (Sect. 4.3), as well as axis ratios (Sect. 4.4) and class fractions (Sect. 4.5). Figures 2 and 4 specifically show how the inferred shape parameters and class fractions evolve with mass and redshift in this work compared to the JWST-CEERS results from table 2 in P24, and the HST-CANDELS results from table 1 in Z19 (accounting for variance and covariance conversions). Because our redshift bins are finer than those of P24 and Z19, and our inference is limited to $0 < z < 1.2$, our bins do not align exactly with theirs. We therefore restrict the comparisons to our $0.6 < z < 1.2$ range, which overlaps with their $0.5 < z < 1.5$ range. There are no uncertainties available for the $M_* = 10^{10}$–$10^{10.5} M_\odot$ bins for Z19 due to their bootstrap algorithm giving unrealistic uncertainties given the small sample size (Z19, section 4.3). In Appendix G, we compute 3D shape class probabilities of individual galaxies from observed b/a and $\log_{10}(a)$ values, and show several example cutouts for each class only for illustrative purposes (Fig. G.1).

4.1. Evolution of 3D ellipticity

In Fig. 2, we show the redshift evolution of mean ellipticity (μ_E; top row) and ellipticity dispersion (σ_E; fourth row) across the three stellar mass bins for $0 < z < 1.2$, compared to Z19 and P24, evaluated at the midpoint of each redshift bin. Similarly to Z19 and P24, we find high mean ellipticities ($\mu_E = 0.600 \pm 0.001$–0.820 ± 0.001) across all mass bins, indicating that most galaxies in the sample are intrinsically non-spherical. Our intrinsic scatter σ_E values are also consistent with both studies, although we find slightly lower values than P24 at $z \sim 0.75$ for low-mass ($M_* = 10^9$–$10^{9.5} M_\odot$) and high-mass ($M_* = 10^{10}$–$10^{10.5} M_\odot$) bins. Across all comparisons, our uncertainties are substantially smaller, reflecting our larger sample: those for μ_E are lower than P24 by a factor of approximately 58–100 and Z19 by 6–27, while those for σ_E are lower by 60–96 and 17–84, respectively. Our additional bins at $0 < z < 0.2$ and $0.2 < z < 0.4$, which extend below the redshift range probed by these earlier studies, show that towards the present day, μ_E continues to rise just above 0.8 across all mass bins, whereas dispersion increases at lower masses.

4.2. Evolution of 3D triaxiality

The second and fifth rows of Fig. 2 show the redshift evolution of the mean triaxiality μ_T and its standard deviation σ_T. We find that in all three mass bins, μ_T decreases towards the present day, and at fixed redshift is higher in low-mass galaxies. P24 typically finds systematically higher μ_T across all mass bins, decreasing over time for low-mass galaxies but rising over time for intermediate- and high-mass galaxies. Z19 reports μ_T values comparable to P24 at $1.0 < z < 1.5$ for the low- and high-mass bins, but lower than both our work and P24 at $0.5 < z < 1.0$ for all bins. Comparisons are more difficult to make quantita-

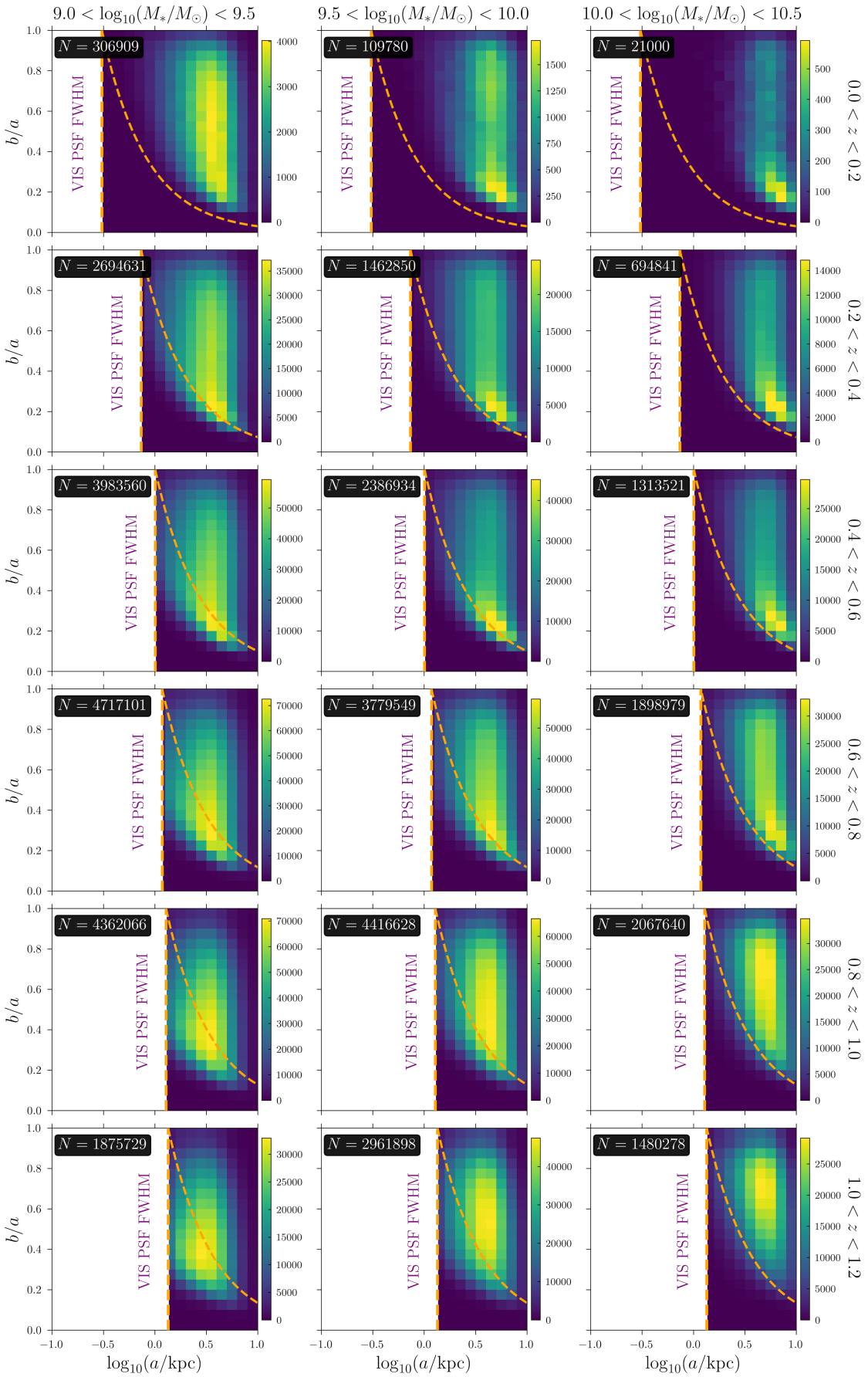


Fig. 1. Projected b/a versus $\log_{10}(a)$ histograms for each mass-redshift bin. The dashed orange line indicates the VIS PSF FWHM converted to units of kiloparsec at the redshift midpoint; the curved portion assumes b = PSF FWHM. Galaxy counts are shown in the top left of each panel.

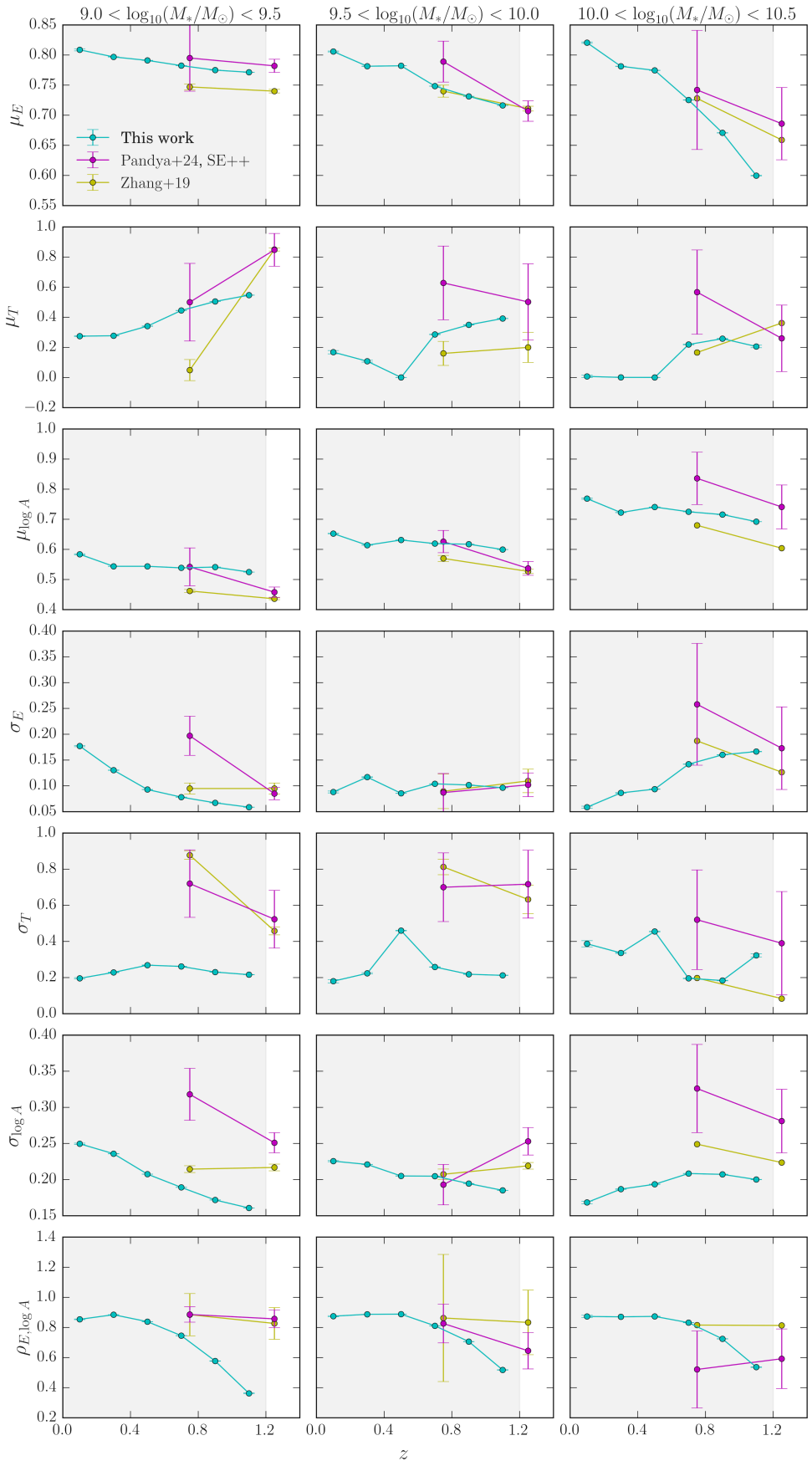


Fig. 2. Comparison of inferred 3D shape parameter evolution with redshift (left to right) and stellar mass in this work (cyan), JWST-CEERS P24 (magenta), and HST-CANDELS Z19 (gold). The shaded region marks this work's redshift coverage ($z \leq 1.2$); points outside it are P24 and Z19's overlapping $1 < z < 1.5$ bin, which overlaps our $0.8 < z < 1.2$ bin. Points show posterior means, with error bars from random draws; Z19 uncertainties are unavailable for high-mass bins due to small sample size.

tively for triaxiality than ellipticity, since the uncertainties in μ_T are much larger in previous studies (by a factor of approximately 25–332 in P24 and 9–30 in Z19), as are the uncertainties in σ_T. Both studies find substantially higher σ_T values than our work in the low- and intermediate-mass bins. At high mass, P24 again shows slightly higher dispersion than our work at $z \sim 0.75$, whereas Z19 is more comparable to ours. Both Z19 and P24 show that σ_T increases from $1.0 < z < 1.5$ to $0.5 < z < 1.0$, our finer redshift bins show that the trend is less constant. We note that P24 break the oblate-prolate degeneracy most effectively for low-mass galaxies at $z > 1$, where they infer $\mu_T \sim 1$ (favouring prolate geometries); as our sample extends only to $z < 1.2$, we do not reach the epoch in which this high-triaxiality, prolate-dominated population dominates.

In the intermediate- and high-mass bins, our results show a dip in μ_T accompanied by a rise in σ_T around $0.4 < z < 0.6$, with the high-mass bin retaining small μ_T for $z < 0.4$. Both parameters remain well constrained here and convergence is good throughout (Table F.1), so this does not indicate a sampling artefact. In these bins μ_T is pinned against the $T = 0$ boundary and σ_T remains large and tightly determined, while in the strongly oblate bins at lower redshift μ_T settles just above zero with a correspondingly small σ_T. The interpretation of this behaviour, and its bearing on the reliability of the inferred triaxialities in these bins, is discussed in Sect. 5.3.

4.3. Evolution of 3D size

The third and sixth rows of Fig. 2 show that the mean 3D size $\mu_{\log_{10}(A)}$ follows the expected mass and redshift scaling, as in Z19 and P24: $\mu_{\log_{10}(A)}$ increases moderately towards the present day, with our additional $0 < z < 0.2$ and $0.2 < z < 0.4$ bins extending this trend to lower redshifts. Our values broadly agree with P24 and Z19 in the low- and intermediate-mass bins; at higher masses, P24 have values slightly higher than ours, while Z19 have values slightly lower. Our size dispersion $\sigma_{\log_{10}(A)}$ values grow slightly towards the present day as mass decreases. In contrast, Z19 find little variation with redshift or mass, and P24 report typically higher values that increase over time for low- and high-mass bins, but decrease at intermediate masses. As before, our uncertainties are markedly smaller: those for $\mu_{\log_{10}(A)}$ are lower than P24 by a factor of approximately 40–162 and Z19 by 5–29, and those for $\sigma_{\log_{10}(A)}$ are lower by 34–172 and 4–56, respectively.

Our $\mu_{\log_{10}(A)}$ values also follow the mild size evolution measured for late-type galaxies by van der Wel et al. (2014b), who find $R_e \propto (1+z)^{-0.75}$ at fixed stellar mass, and our $\sigma_{\log_{10}(A)}$ values are of the same order as the intrinsic scatter of ~ 0.16–0.19 dex they measure in $\log_{10}(R_e/\mathrm{kpc})$ at fixed mass, which is nearly independent of both mass and redshift (noting that their scatter refers to projected sizes at fixed mass rather than intrinsic 3D sizes within a mass bin).

The last row of Fig. 2 shows the evolution of $\rho_{E,\log_{10}(A)}$, the correlation between 3D ellipticity and size. We find with small uncertainties that $\rho_{E,\log_{10}(A)}$ increases towards the present day in all mass bins, reaching present-day values of 0.854 ± 0.002–0.875 ± 0.003. Z19 find a roughly constant correlation for all mass-redshift bins with values similar to our present-day ones (though with substantial uncertainties, particularly at intermediate masses), while P24 find that this correlation becomes slightly stronger over time as mass decreases (with larger uncertainties at higher masses). This positive correlation indicates that larger galaxies tend to have higher intrinsic ellipticities (more flattened), consistent with galaxies growing in size and settling into progressively more disc-like configurations over time.

4.4. Evolution of 3D axis ratios

From the seven inferred population-level shape parameters, we draw random samples from the trivariate Gaussian for each mass–redshift bin and place them in 3D C/A–B/A axis-ratio space. This is shown in Fig. 3, where each distribution is constructed from the average of 500 random posterior draws, and the prolate, oblate, and spheroidal regions are delineated by the boundaries (in yellow) following figure 1 of Z19 and figure 2 of vdW14a. We then compute the fraction of samples that fall into each of the shape regions. Given that a different choice in boundaries would ultimately yield different fractions, these should therefore be read as a convenient summary of the inferred distributions rather than as directly constrained observables. The evolution described in the previous sections is also apparent here: all three mass bins converge towards the oblate region by the present day, but from distinct high-redshift starting points: near the prolate-oblate intersection at low mass, the spheroid-oblate boundary at intermediate mass, and a broad spread across spheroidal and oblate geometries at high mass.

4.5. Evolution of 3D shape fractions

The evolution of the inferred population-level 3D shape fractions for each mass–redshift bin, from random posterior draws and compared to P24, is shown in Fig. 4. In addition, analogous to figure 4 of vdW14a, figure 13 of Z19, and figure 16 of P24, our Fig. 5 shows stacked histograms of the inferred 3D shape fractions using the total posterior means rather than random draws.

The low-mass prolate fraction shows the best agreement with Z19 and P24, decreasing steadily towards the present day. Our additional $0 < z < 0.2$ and $0.2 < z < 0.4$ bins show that this decline continues, approaching a near-negligible level by $z \sim 0$. At intermediate masses, we find lower prolate fractions than in either study, and at high masses our prolate fraction is lower than P24 but higher than the near-zero values of Z19.

The oblate fractions show the inverse trend, steadily increasing towards the present day in all mass bins. Our values exceed those of P24 across all mass bins and those of Z19 at low and intermediate masses. Z19 and P24 agree well with each other at low and intermediate masses, but both fall below our values. At $z \sim 0.75$, our oblate fraction and that of Z19 are both around 70%. The exception to the rising trend is the low-mass bin, where the oblate fraction dips slightly from 0.798 ± 0.001 at $0.2 < z < 0.4$ to 0.763 ± 0.003 at $0 < z < 0.2$. In the intermediate-mass bin at $z \sim 0$, nearly all galaxies are classified as oblate.

In the low-mass bin, our spheroid fractions rise towards the present day, from a near-negligible level to 0.194 ± 0.002 at $0 < z < 0.2$. Compared to Z19 and P24, our spheroid fractions are broadly consistent in intermediate masses and slightly lower in low masses; in high masses, they are consistent at $0.8 < z < 1.0$ but slightly higher than both studies at $1.0 < z < 1.2$. Notably, all three studies find elevated spheroid fractions at high masses for a nominally star-forming sample, despite the expectation that genuine star-forming spheroids should be rare (Sect. 5.1). We caution that these fractions are sensitive to the breadth of the inferred distribution rather than being directly constrained; because the classes are assigned a posteriori by sampling the trivariate Gaussian, a broad inferred distribution (large σ_E or σ_T) scatters more samples into the spheroidal region of the C/A–B/A plane, which

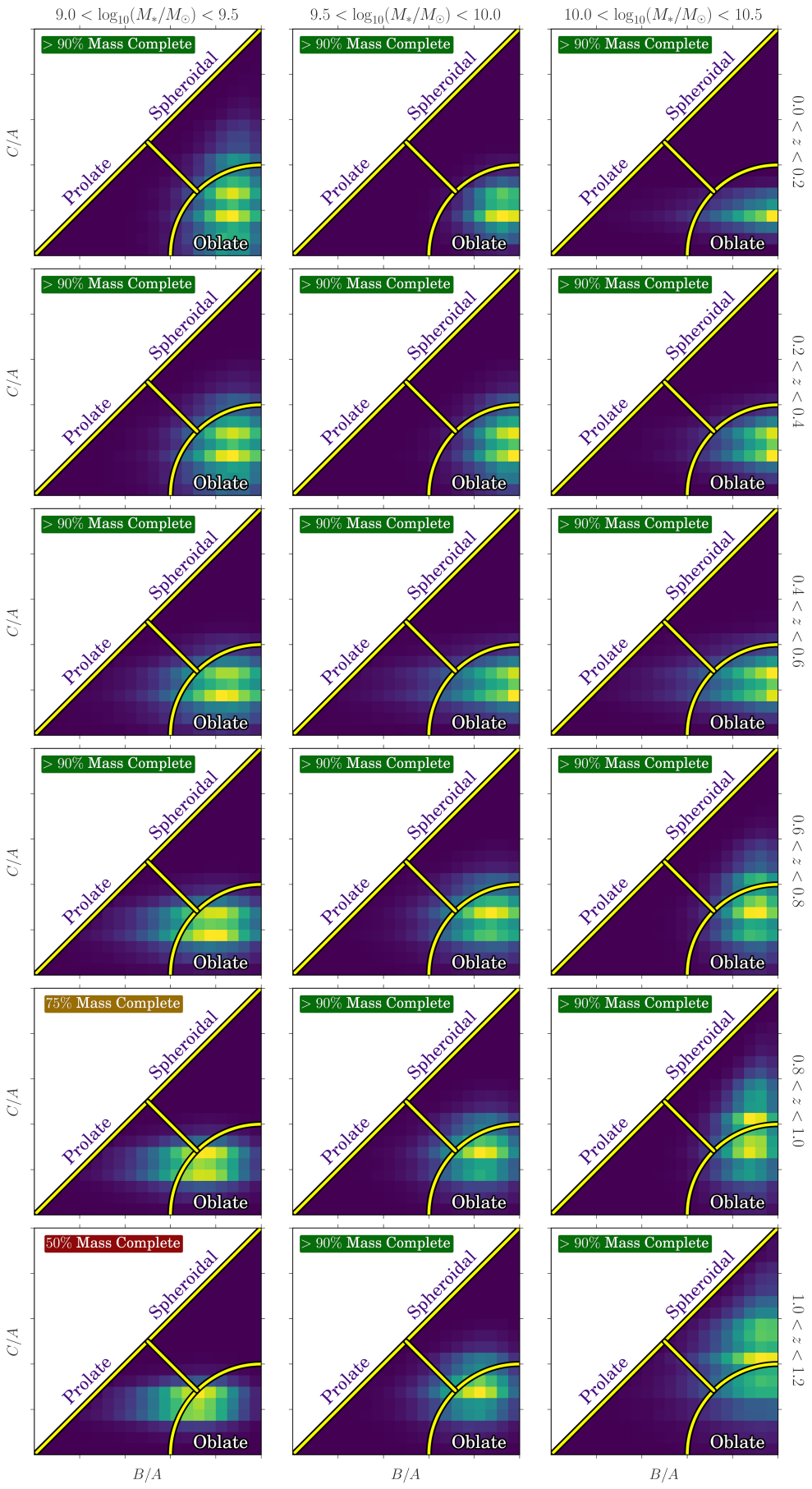


Fig. 3. Predicted C/A versus B/A axis-ratio distributions averaged from posterior draws for each mass-redshift bin. 3D shape boundaries (in yellow) follow figure 1 of vdW14a and figure 2 of Z19. Mass completeness is labelled for each bin (top left; Appendix E).

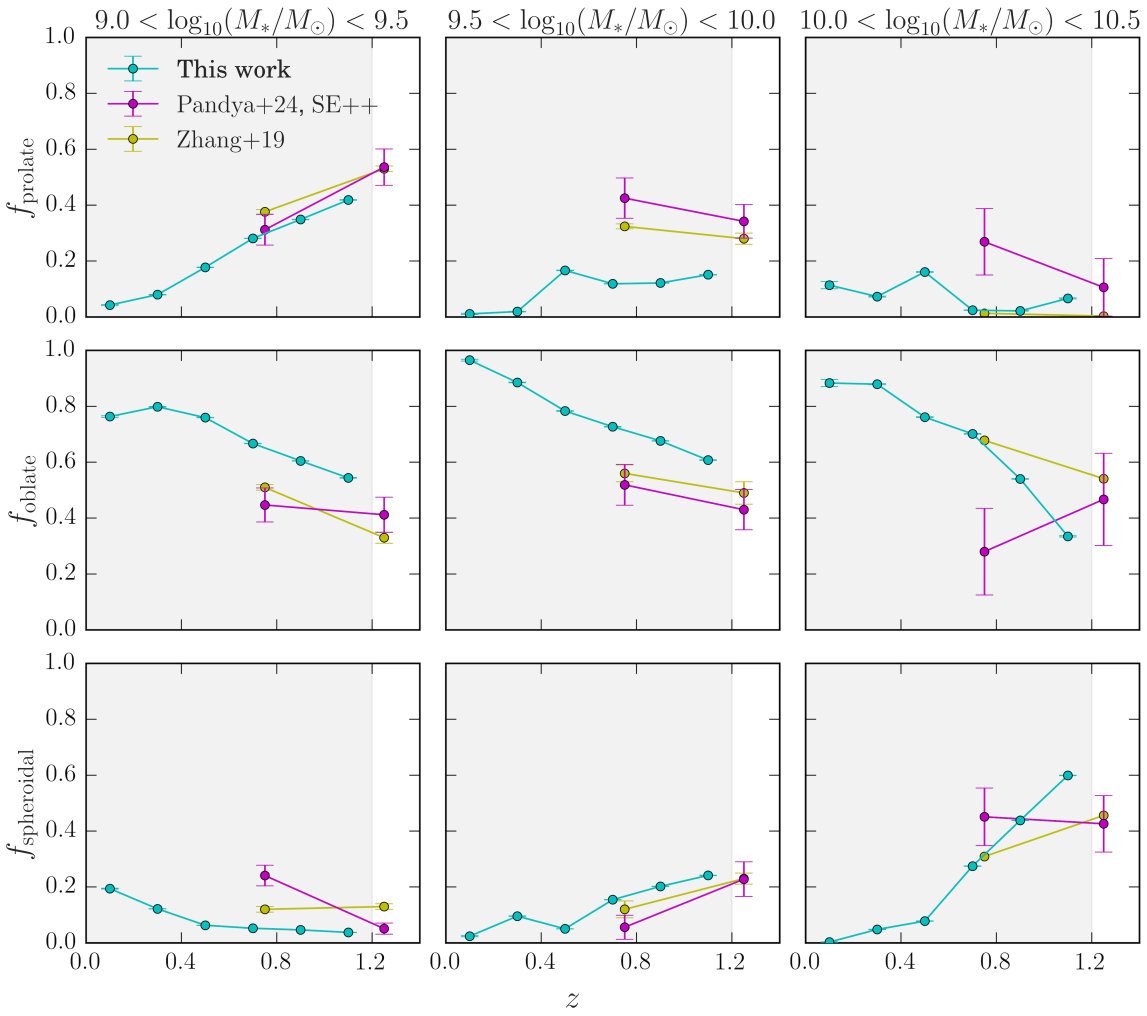


Fig. 4. Similar to Fig. 2, but showing the evolution of population-level inferred 3D shape fractions with redshift and mass.

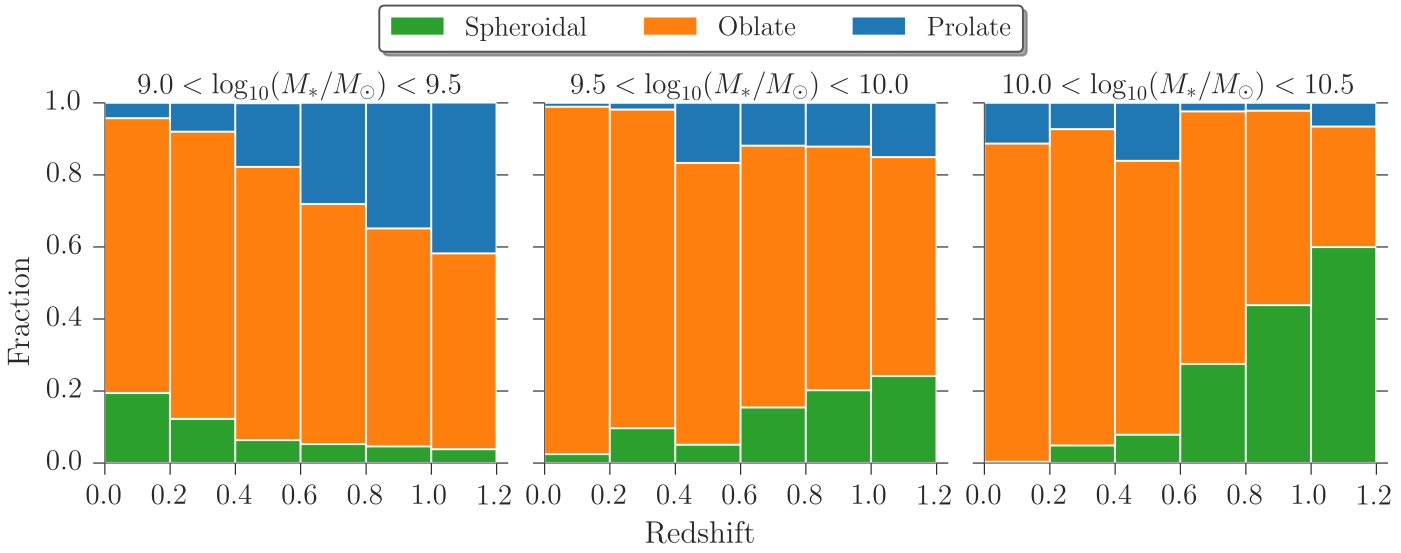


Fig. 5. Similar to Fig. 4, but showing per-bin 3D shape fractions computed from full posterior means rather than random draws. The shaded region again marks this work's redshift coverage ($z \leq 1.2$).

can inflate the spheroid fraction even where the mean shape is disc-like. This is the same broadening responsible for the boundary behaviour of σ_T discussed in Sect. 4.2, and is most pronounced in the high-mass bins where the inferred dispersions are largest.

5. Discussion

In this section, we further compare our findings with previous studies (Sect. 5.1), discuss the astrophysical implications (Sect. 5.2), acknowledge key limitations (Sect. 5.3), and outline recommendations for future work (Sect. 5.4).

5.1. Comparison with previous studies

Having briefly compared our posterior-draw results with those from P24 and Zhang et al. (2019) in Sect. 4, we now focus on comparative results between this work, vdW14a, Z19, and P24 in more depth. Given that our redshift bins do not align with those used in these studies, the following comparisons are made at the trend level rather than bin by bin.

For the low-mass bin, our *Euclid*-based findings show a strongly oblate-dominated population at all redshifts, with the oblate fraction steadily increasing towards the present day, while the prolate fraction decreases. This matches the qualitative behaviour in vdW14a, Z19, and P24. However, our oblate fraction is visibly higher, and our prolate fraction lower, than Z19 and P24 in the overlapping redshift range; the oblate fraction in vdW14a, which extends to $0 < z < 0.5$, is greater than in the other studies, with near-zero prolate and spheroid fractions. As noted in Sect. 4.2, P24 break the oblate-prolate degeneracy most effectively for low-mass galaxies at $z > 1$, where the prolate-dominated population yields $\mu_T \sim 1$. Since our sample extends only to $z < 1.2$, our overlapping comparison samples the later epoch in which their inferred prolate fraction has already declined and discs have begun to dominate; our lower prolate fractions and triaxialities at low mass are therefore consistent with their evolutionary trend. In this sense, our results support the low-redshift, disc-settled end of the same prolate-to-oblate transition that P24 trace towards its high-redshift, prolate-dominated origin. Spheroid fractions are very small, rising modestly towards the present day. In overlapping redshift bins, these fractions are fairly consistent with the small values seen in P24 and Z19.

For intermediate-mass galaxies, our population is again overwhelmingly oblate – broadly consistent with the oblate dominance in the other studies – increasing to nearly unity by the present day, with a similar ratio to Z19 and P24 as low-mass bins. Prolate fractions remain lower than Z19 and P24, and are more comparable to the values of vdW14a. Our spheroid fractions are again low, decreasing towards the present day, similarly to vdW14a, P24, and Z19. The high-mass bin also shows oblate dominance over time, and is the only bin in our grid where spheroids are the dominant class at higher redshifts. This substantial spheroid population is found in all three studies at higher masses. Like vdW14a, our $0 < z < 0.2$ and $0.2 < z < 0.4$ bins reveal that the spheroid fraction continues to decline towards the present day, beyond where the bins in Z19 and P24 end.

Overall, the most notable agreement is the prolate-to-oblate transition at low masses seen consistently in all studies. Our much larger sample suggests that this trend may be a genuine feature of star-forming galaxy evolution rather than an artefact of small-sample statistics. The increase in spheroid fractions with mass is also qualitatively consistent across all three studies. The offsets in central values for the seven shape parameters between this work and vdW14a, Z19, and P24 probably stem from a combination differences in instrument, wavelength coverage, and selection function. The most important precision difference seems to be our substantially larger sample, which yields far tighter constraints on the inferred shape distributions. Our own experience illustrates this directly: applying the same method to a smaller sample of 929 344 star-forming galaxies from Euclid Quick Data Release 1 (Q1; Euclid Quick Release Q1 2025; Euclid Collaboration: Aussel et al. 2026) produced posteriors that struggled to converge in many bins – mainly for triaxiality – whereas the DR1 Wide sample used here yields well-converged inferences across all bins. In a future paper, we plan to incorporate *Euclid* near-infrared (NIR) imaging ($Y_{\rm E}$, $J_{\rm E}$, $H_{\rm E}$; Euclid Collaboration: Jahnke et al. 2025; Euclid Collaboration: Polenta et al., in prep.) into this analysis, both to mitigate the surface-brightness and wavelength-dependent biases inherent to VIS-only shape measurements, and to test whether the agreement among studies persists towards higher redshifts, where rest-frame optical morphology shifts into the near-infrared.

5.2. Astrophysical implications

The observed prolate-to-oblate evolutionary transition in low-mass galaxies is consistent with the theoretical framework of Pandya et al. (2019) and with predictions from zoom-in cosmological simulations (Ceverino et al. 2015; Tomassetti et al. 2016). In this picture, high-redshift prolate dwarfs form within elongated dark matter haloes embedded in cosmic filaments, undergoing repeated mergers along the filament direction that maintain their elongated geometries and produce intrinsic alignments with large-scale structure. Ceverino et al. (2015) and Tomassetti et al. (2016) further predict that high-redshift galaxies undergo 'compaction events', in which rapid gas inflows shift galaxy centres from dark-matter–dominated to baryon-dominated configurations capable of supporting stable discs (Lapiner et al. 2023). Dekel et al. (2020) show that gas discs are expected to persist only in haloes above a threshold of $2 \times 10^{11}\,M_{\odot}$ (corresponding to a stellar mass of approximately $10^{9} M_{\odot}$, with little redshift dependence), below which repeated mergers and dark-matter dominance disrupt early discs before they can stabilise. This threshold sits at the low-mass end of our sample and is consistent with the prolate phase persisting longest in our lowest-mass bins, where disc disruption is expected to dominate. As these systems evolve, gas accretion and compaction enable disc formation, driving the transition towards oblate-dominated populations. Our substantial disc fractions across all masses and redshifts, which increase towards the present day, indicate that disc structures begin to establish themselves relatively early, even as the transition to oblate dominance continues to low redshift. However, distinguishing genuine oblate discs from other morphologies remains a challenge. Recent work by Pandya et al. (2025) found preliminary evidence for non-random orientations in JWST-CEERS data via weak lensing, supporting the filament-alignment scenario, while Hasan et al. (2026) confirmed using TNG50 simulations that prolate galaxies preferentially inhabit low-density, recently collapsing filaments with strong alignments, potentially detectable with the *Roman* Space Telescope or *Euclid*.

As in both Z19 and P24, our nominally prolate bins frequently occupy the triaxial rather than the extreme prolate region of C/A–B/A space (Fig. 3), indicating more oval flattened discs rather than purely elongated ellipsoids. This is consistent with a picture in which high-z star-forming galaxies undergo disc settling along two axes simultaneously – from both thick-to-thin *and* oval-to-circular – as gas dissipates and angular momentum builds over time (Elmegreen et al. 2005; Law et al. 2012; Pandya et al. 2024). Our positive $\rho_{E,\log_{10}(A)}$ values link the size growth of star-forming galaxies at fixed stellar mass (van der Wel et al. 2014b) directly to increasing intrinsic flattening, consistent with discs settling as they grow. As noted in Sect. 5.1, our predicted

spheroid fractions and their trends appear to be broadly consistent with the other previous inference studies. Although HST-based observations suggest that star-forming spheroids should be rare (Brennan et al. 2015), moderate spheroid fractions are found at higher masses at higher redshifts. As speculated in section 6.2 of P24, if these fractions are real, they may reflect the same compaction processes invoked above, but channelled towards spheroid formation rather than disc settling: gas-rich mergers, disc instabilities, or cold gas inflows drive a rapid increase in central mass surface density prior to quenching (Dekel & Burkert 2014; Zolotov et al. 2015; Tacchella et al. 2016; Lapiner et al. 2023).

We also compare to predictions from the TNG50 hydrodynamical simulations at $z = 0.5$ and $z = 2$ (figure 8 of Pillepich et al. 2019). In agreement with our results, TNG50 predicts a higher prolate fraction at $z = 2$ than at $z = 0.5$ across all masses; however, it also predicts a correspondingly larger high-redshift spheroid fraction at all masses, whereas we recover this trend only for $\log_{10}(M_*/M_\odot) > 9.5$. At $z = 0.5$, Pillepich et al. (2019) predict essentially no prolate galaxies, yet we find prolate fractions of approximately 16–18% in every mass bin. This discrepancy echoes earlier findings from vdW14a, Z19, and P24, and probably reflects limitations in simulation physics, observational systematics in how shapes are measured and classified, and genuine differences between simulated and real galaxy populations.

5.3. Limitations of the study

The larger statistical sample of DR1 enables tighter constraints on 3D shape distributions than previous inference studies. However, several methodological choices and observational limitations warrant careful consideration.

Our inference uses global single-Sérsic axis ratios and sizes, which describe the flux-weighted projected shape of the whole light distribution rather than that of individual galaxy components (e.g., bulges and discs, bars, spiral arms). For bulge+disc systems, the global axis ratio closely follows that of the disc for face-on galaxies and for a bulge-to-total light ratio $\mathrm{B/T} \lesssim 0.1$, differing significantly only for edge-on discs with substantial bulges (Quilley et al. 2026). In those cases, the bulge raises b/a without reducing the projected size, which can shift the inference towards thicker oblate or spheroidal geometries rather than prolate ones, since prolate populations are identified mainly through round projections at small sizes. Our sample is restricted to star-forming galaxies, for which B/T is typically low (Dimauro et al. 2022; Shuntov et al. 2026; Yang et al. 2026); the median Sérsic index in our lowest-mass bins is $n \approx 1.1$. Sérsic axis ratios and sizes are typically recovered without significant bias down to $\mathrm{S/N} \approx 20$, independent of depth and resolution (e.g., Häussler et al. 2007; Guo et al. 2009; van Der Wel et al. 2012; Bruce et al. 2012; Sazonova et al. 2026), and our comparisons with HST and isophotal-based measurements (Appendix B) show that the axis ratios remain reliable to $I_E = 24.5$. Nevertheless, galaxies with several components may be poorly approximated by a single 3D ellipsoid, and non-parametric measures or multi-component fits could provide complementary constraints.

Single-source catalogues may also conflate multiple objects into one. Close pairs or small groups (whether physically associated or merely aligned in projection) along with interacting or merging systems, can be fit as a single galaxy, producing anomalous projected axis ratios and sizes that do not correspond to any single intrinsic ellipsoid. Because both the physical merger rate and the line-of-sight projection probability increase with redshift, the prevalence of such blends is expected to vary across our bins, potentially introducing a redshift-dependent systematic. This may already affect our highest-redshift bins, and will become considerably more significant as we extend the analysis to higher redshifts in future work, where blending and merger confusion are increasingly common. Deep-learning morphology classifiers such as `Zoobot` (Walmsley et al. 2023; Euclid Collaboration: Walmsley et al. 2026) could help identify mergers, interacting systems, and blended sources before inference.

As noted in Sect. 3.1, our choice to retain only galaxies larger than the PSF FWHM ensures that resolved sources dominate the analysis. However, it may systematically exclude rounder, more compact, high-surface-brightness objects, shifting the inferred sizes upward and biasing the shape distributions – particularly at high redshift and low masses, where such objects are most common.

Our reliance on the single I_E broadband filter also means that we probe different rest-frame wavelengths as a function of redshift, which is in large part why we restrict the present analysis to $0 < z < 1.2$. Over this range, I_E still samples at or near the optical rest-frame, where structural measurements best trace the underlying stellar-mass distribution. At higher redshifts, the band shifts into rest-frame UV, which increasingly traces clumpy, unobscured star formation rather than the bulk stellar light. Dust attenuation compounds this effect: because attenuation is strongest at short wavelengths and our star-forming sample is comparatively dust-rich, an inclination-dependent reddening can alter a galaxy's apparent ellipticity and size. An edge-on disc, for instance, suffers far more attenuation along the line of sight than the same disc seen face-on. As our rest-frame coverage shifts blueward with increasing redshift, this attenuation grows, so dust may bias not only the measured shapes but also their apparent evolution with redshift (Padilla & Strauss 2008; Zhang et al. 2019, 2023). P24 mitigated this by selecting JWST Near Infrared Camera (NIRCam) filters that maintain consistent rest-frame coverage across redshift. Incorporating NIR imaging in future work would maintain rest-frame optical coverage to higher redshift, ultimately enabling a robust extension of this analysis beyond $z \sim 1$. This would also allow us to independently test the breaking of oblate-prolate degeneracy that occurs at $z > 1$ in P24.

The most fundamental assumption underlying our approach is that, within each bin of stellar mass and redshift, the galaxy population is well described by a single parent 3D shape distribution, of which the observed projected axis ratios and sizes are realisations (Sect. 2). The inference constrains the seven parameters of this distribution, but cannot uniquely recover the 3D shape of any individual galaxy, since a given projected b/a and $\log_{10}(a)$ is consistent with a range of intrinsic geometries viewed at different angles. The class fractions we report are likewise not inferred quantities, but computed by partitioning samples of the inferred distribution in the C/A–B/A plane, and depend on the placement of class boundaries. They should therefore be read as summaries of the underlying shape parameters, not as independent constraints.

A related caution applies to the shape parameters themselves. Triaxiality is the most sensitive to our modelling assumptions, since it is recovered indirectly from the projected b/a–$\log_{10}(a)$ distribution rather than constrained by any direct observable, and tight statistical constraints do not guarantee freedom from systematic bias by themselves. The single trivariate Gaussian enforces a unimodal triaxiality distribution within each bin; where the true population is instead a mixture of distinct geometric families – for example a near-oblate ($T \simeq 0$) component alongside a more triaxial one – the inferred μ_T and σ_T blend the two

rather than resolving them. This is evident in the intermediate- and high-mass bins, where μ_T is pinned at the $T = 0$ boundary while σ_T is simultaneously large and tightly determined (Sect. 4.2). The model can reproduce a broad, boundary hugging distribution only by placing its mean on the boundary and widening its dispersion. In these regimes, a precisely determined μ_T should not be read as an accurate one. We stress that this concerns the detailed triaxiality within these specific bins, not the robust oblate dominance itself, which is driven by the ellipticity and axis-ratio structure rather than by μ_T. Sampling directly in C/A–B/A space may avoid this, since the oblate region does not lie against a parameter boundary there; alternatively, a mixture model separating oblate and triaxial subpopulations would recover both components rather than averaging over them. Either change would require new model libraries and more complex models, for which methods more scalable than HMC may be necessary.

A key practical limitation is computational cost. Although HMC is far more efficient than traditional MCMC, inference can still take days per DR1 bin on a computing cluster. Scaling to larger data sets or performing extensive tests to address the aforementioned limitations would be computationally prohibitive, motivating the need for faster alternative methods.

5.4. Future directions

This work recovers established evolutionary trends through improved statistics while highlighting several avenues for further progress, both scientific and methodological. Combining VIS and NIR imaging will help mitigate the biases inherent to single-band VIS shape measurements and extend the analysis to higher redshifts, yielding better-constrained shapes across the full sample. Future *Euclid* releases reaching fainter magnitudes will enable finer redshift and mass binning, allowing evolutionary transitions to be traced more precisely. Connecting galaxy 3D shapes to the cosmic web would further reveal how these distributions vary with environment and large-scale structure. However, realising this potential across future *Euclid* releases and other large surveys (e.g. LSST, *Roman*) will require overcoming the computational cost per-bin that currently limits this approach. Simulation-based inference (SBI) offers a promising path: neural density estimators trained on simulated observations make posterior estimation nearly instantaneous, converting a recurring bottleneck into a one-off training cost. We plan to explore these in a forthcoming paper.

6. Conclusions

We applied the Bayesian inference framework of P24 to 40 864 304 DR1 Wide star-forming galaxies with $I_E \leq 24.5$ across bins of stellar mass $\log_{10}(M_*/M_\odot) = 9.0$–$10.5$ at photometric redshifts $0 < z < 1.2$. Using Sérsic axis ratios and semi-major axes from VIS imaging, we constrained the population-level mean 3D ellipticity, triaxiality, and size, together with their covariance, and derived the fractions of galaxies classified as prolate, oblate, or spheroidal in each mass-redshift bin. We demonstrated that this methodology scales reliably to the tens of millions of galaxies in DR1 while recovering the evolutionary trends of previous studies. Our main conclusions are as follows:

- Low-mass star-forming galaxies appear to evolve from predominantly prolate to oblate geometries towards the present day. This trend is consistent with comparable analyses from vdW14a, Z19, and P24, despite differences in instrument, wavelength, and selection; this suggests it is not an artefact of small-sample statistics, but potentially a genuine feature of star-forming galaxy evolution.
- Across all stellar masses, the oblate fraction increases towards $z = 0$, eventually becoming the dominant class. For higher masses, spheroids constitute a substantial fraction at higher redshifts before declining towards the present day.
- Our DR1 sample significantly reduces the uncertainties in inferred 3D shape parameters compared to Z19 and P24, and our additional bins at $z < 0.5$ extend the observed trends seen in these studies towards the present day.
- Even where galaxies are nominally classified as prolate, they frequently occupy the triaxial region of C/A–B/A space, indicating more oval, flattened discs rather than purely elongated ellipsoids. This is consistent with a two-axis disc-settling picture for high-z star-forming galaxies.

Future *Euclid* releases reaching fainter magnitudes will improve stellar-mass completeness, enable finer mass-redshift binning, and facilitate detailed studies of morphology versus environment. Scaling to larger samples with more efficient inference methods, together with addressing the principal limitations identified here, is deferred to a forthcoming paper.

Acknowledgements. Funded by the European Union (MSCA Doctoral Network EDUCADO, GA 101119830 and Widening Participation, ExGal-Twin, GA 101158446). Views and opinions expressed are however those of the author(s) only and do not necessarily reflect those of the European Union. Neither the European Union nor the granting authority can be held responsible for them. JHK acknowledges grant PID2022-136505NB-I00 funded by MCIN/AEI/10.13039/501100011033 and EU, ERDF. This work is part of grant CEX2025-001609-S, awarded to the Instituto de Astrofísica de Canarias under the Severo Ochoa Centre of Excellence program and funded by MICIU/AEI/10.13039/501100011033. This work has made use of the Euclid Data Release 1 (DR1) from the European Space Agency (ESA) mission *Euclid*, available at https://www.cosmos.esa.int/web/euclid/data-release-dr1. The Euclid Consortium acknowledges the European Space Agency and a number of agencies and institutes that have supported the development of *Euclid*, in particular the Agenzia Spaziale Italiana, the Austrian Forschungsförderungsgesellschaft funded through BMIMI, the Belgian Science Policy, the Canadian Euclid Consortium, the Deutsches Zentrum für Luft- und Raumfahrt, the DTU Space and the Niels Bohr Institute in Denmark, the French Centre National d'Etudes Spatiales, the Fundação para a Ciência e a Tecnologia, the Hungarian Academy of Sciences, the Ministerio de Ciencia, Innovación y Universidades, the National Aeronautics and Space Administration, the National Astronomical Observatory of Japan, the Netherlandse Onderzoekschool Voor Astronomie, the Norwegian Space Agency, the Research Council of Finland, the Romanian Space Agency, the Swiss Space Office (SSO) at the State Secretariat for Education, Research, and Innovation (SERI), and the United Kingdom Space Agency. A complete and detailed list is available on the *Euclid* web site (www.euclid-ec.org/consortium/community/). This research makes use of ESA Datalabs (datalabs.esa.int), an initiative by ESA's Data Science and Archives Division in the Science and Operations Department, Directorate of Science. This work was made possible by utilising the CANDIDE cluster at the Institut d'Astrophysique de Paris. The cluster was funded through grants from the PNCG, CNES, DIM-ACAV, the Euclid Consortium, and the Danish National Research Foundation Cosmic Dawn Center (DNRF140). It is maintained by Stephane Rouberol. The author(s) also wish to acknowledge the contribution of Teide High-Performance Computing facilities to the results of this research. TeideHPC facilities are provided by the Instituto Tecnológico y de Energías Renovables (ITER, SA). URL: https://teidehpc.iter.es.

References

Alam, S. M. K. & Ryden, B. S. 2002, ApJ, 570, 610
Barden, M., Häußler, B., Peng, C. Y., McIntosh, D. H., & Guo, Y. 2012, MNRAS, 422, 449
Bertin, E., Schefer, M., Apostolakos, N., et al. 2020, in ASP Conf. Ser., Vol. 527, Astronomical Data Analysis Software and Systems XXIX, ed. R. Pizzo, E. R. Deul, J. D. Mol, J. de Plaa, & H. Verkouter, 461
Betancourt, M. 2016, arXiv:1604.00695
Binney, J. 1978, MNRAS, 183, 501

Binney, J. 1985, MNRAS, 212, 767
Brennan, R., Pandya, V., Somerville, R. S., et al. 2015, MNRAS, 451, 2933
Bruce, V. A., Dunlop, J. S., Cirasuolo, M., et al. 2012, MNRAS, 427, 1666
Caldwell, N. 1983, AJ, 88, 804
Cappellari, M. 2016, ARA&A, 54, 597
Ceverino, D., Primack, J., & Dekel, A. 2015, MNRAS, 453, 408
Chang, Y.-Y., van der Wel, A., Rix, H.-W., et al. 2013, ApJ, 773, 149
Contopoulos, G. 1956, ZAp, 39, 126
Costantin, L., Méndez-Abreu, J., Corsini, E. M., et al. 2018, A&A, 609, A132
Cowie, L. L., Hu, E. M., & Songaila, A. 1995, AJ, 110, 1576
de Vaucouleurs, G. 1959, HDP, 53, 311
Dekel, A. & Burkert, A. 2014, MNRAS, 438, 1870
Dekel, A., Ginzburg, O., Jiang, F., et al. 2020, MNRAS, 493, 4126
Dimauro, P., Daddi, E., Shankar, F., et al. 2022, MNRAS, 513, 256
Elmegreen, D. M., Elmegreen, B. G., & Hirst, A. C. 2004a, ApJ, 604, L21
Elmegreen, D. M., Elmegreen, B. G., Rubin, D. S., & Schaffer, M. A. 2005, ApJ, 631, 85
Elmegreen, D. M., Elmegreen, B. G., & Sheets, C. M. 2004b, ApJ, 603, 74
Emsellem, E., Cappellari, M., Krajnović, D., et al. 2011, MNRAS, 414, 888
Euclid Collaboration: Aussel, H., Tereno, I., Schirmer, M., et al. 2026, A&A, 711, A1
Euclid Collaboration: Bretonnière, H., Kuchner, U., Huertas-Company, M., et al. 2023, A&A, 671, A102
Euclid Collaboration: Cropper, M., Al-Bahlawan, A., Amiaux, J., et al. 2025, A&A, 697, A2
Euclid Collaboration: Jahnke, K., Gillard, W., Schirmer, M., et al. 2025, A&A, 697, A3
Euclid Collaboration: Mellier, Y., Abdurro'uf, Acevedo Barroso, J., et al. 2025, A&A, 697, A1
Euclid Collaboration: Merlin, E., Castellano, M., Bretonnière, H., et al. 2023, A&A, 671, A101
Euclid Collaboration: Quilley, L., Damjanov, I., de Lapparent, V., et al. 2026, A&A, 711, A8
Euclid Collaboration: Scaramella, R., Amiaux, J., Mellier, Y., et al. 2022, A&A, 662, A112
Euclid Collaboration: Walmsley, M., Huertas-Company, M., Quilley, L., et al. 2026, A&A, 711, A9
Euclid Data Release 1. 2026, https://doi.org/10.57780/esa-d079c51
Euclid Quick Release Q1. 2025, https://doi.org/10.57780/esa-2853f3b
Ferguson, H. C. & Binggeli, B. 1994, A&A Rev., 6, 67
Ferguson, H. C. & Sandage, A. 1989, ApJ, 346, L53
Finkelstein, S. L., Bagley, M. B., Ferguson, H. C., et al. 2023, ApJ, 946, L13
Flegal, J. & Jones, G. 2011, Implementing MCMC: Estimating with confidence (United States: CRC Press), 175–198
Flegal, J. M. & Jones, G. L. 2010, Ann. Stat., 38
Foreman-Mackey, D. 2016, JOSS, 1, 24
Franx, M., Illingworth, G., & De Zeeuw, T. 1991, ApJ, 383, 112
Gelman, A., Carlin, J. B., Stern, H. S., et al. 2013, Bayesian Data Analysis, 3rd edn. (Boca Raton, FL: CRC Press)
Gómez, P., Ruhberg, L. E., Anett Remmelgas, K., & O'Ryan, D. 2025, arXiv:2511.04429
Gong, L. & Flegal, J. M. 2016, JCJS, 25, 684–700
Griffith, R. L., Cooper, M. C., Newman, J. A., et al. 2012, ApJS, 200, 9
Grogin, N. A., Kocevski, D. D., Faber, S. M., et al. 2011, ApJS, 197, 35
Guo, Y., McIntosh, D. H., Mo, H. J., et al. 2009, MNRAS, 398, 1129–1149
Hamilton-Campos, K. A., Simons, R. C., Peeples, M. S., Snyder, G. F., & Heckman, T. M. 2023, ApJ, 956, 147
Hasan, F., Zhang, H., Pandya, V., et al. 2026, ApJ, 1004, 74
Hoffman, M. D. & Gelman, A. 2014, JMLR, 15, 1593
Hoffmann, K., Laigle, C., Chisari, N. E., et al. 2022, MNRAS, 515, 3603
Hubble, E. P. 1926, ApJ, 64, 321
Häussler, B., McIntosh, D. H., Barden, M., et al. 2007, ApJS, 172, 615
Ichikawa, S.-I., Wakamatsu, K.-I., & Okamura, S. 1986, ApJS, 60, 475
Kado-Fong, E., Petrescu, M., Mohammad, M., et al. 2021, ApJ, 920, 72
Koekemoer, A. M., Faber, S. M., Ferguson, H. C., et al. 2011, ApJS, 197, 36
Kümmel, M., Álvarez-Ayllón, A., Bertin, E., et al. 2022, arXiv:2212.02428
Lambas, D. G., Maddox, S. J., & Loveday, J. 1992, MNRAS, 258, 404
Lapiner, S., Dekel, A., Freundlich, J., et al. 2023, MNRAS, 522, 4515
Law, D. R., Steidel, C. C., Shapley, A. E., et al. 2012, ApJ, 745, 85
Méndez-Abreu, J., Simonneau, E., Aguerri, J. A. L., & Corsini, E. M. 2010, A&A, 521, A71
Navarro, V., del Rio, S., Angel Diego, M., et al. 2024, in Space Data Management. Studies in Big Data, Vol. 141, 1–13
Noerdlinger, P. D. 1979, ApJ, 234, 802
Oke, J. B. 1974, ApJS, 27, 21
Padilla, N. D. & Strauss, M. A. 2008, MNRAS, 388, 1321
Pandya, V., Brennan, R., Somerville, R. S., et al. 2017, MNRAS, 472, 2054
Pandya, V., Loeb, A., McGrath, E. J., et al. 2025, ApJ, 986, 72
Pandya, V., Primack, J., Behroozi, P., et al. 2019, MNRAS, 488, 5580
Pandya, V., Zhang, H., Huertas-Company, M., et al. 2024, ApJ, 963, 54
Pillepich, A., Nelson, D., Springel, V., et al. 2019, MNRAS, 490, 3196
Planck Collaboration, Ade, P. A. R., Aghanim, N., et al. 2016, A&A, 594, 63
Pozzetti, L., Bolzonella, M., Zucca, E., et al. 2010, A&A, 523, A13
Quilley, L., de Lapparent, V., Bolzonella, M., et al. 2026, A&A, 710, A277
Ravindranath, S., Giavalisco, M., Ferguson, H. C., et al. 2006, ApJ, 652, 963
Rix, H.-W., Barden, M., Beckwith, S. V. W., et al. 2004, ApJS, 152, 163
Rix, H.-W. & Zaritsky, D. 1995, ApJ, 447, 82
Rodríguez, S. & Padilla, N. D. 2013, MNRAS, 434, 2153
Ryden, B. 1992, ApJ, 396, 445
Ryden, B. S. 2004, ApJ, 601, 214
Salvatier, J., Wiecki, T. V., & Fonnesbeck, C. 2016, PeerJ Comput. Sci., 2, e55
Sánchez-Janssen, R., Méndez-Abreu, J., & Aguerri, J. A. L. 2010, MNRAS, 406, L65
Sandage, A. 1961, The Hubble Atlas of Galaxies (Carnegie Institution of Washington)
Sandage, A., Freeman, K. C., & Stokes, N. R. 1970, ApJ, 160, 831
Sazonova, E., Morgan, C. R., Balogh, M., et al. 2026, OJAp, 9
Scoville, N., Aussel, H., Brusa, M., et al. 2007, ApJS, 172, 1
Sérsic, J. L. 1963, BAAA, 6, 41
Shuntov, M., Ilbert, O., Del P. Lagos, C., et al. 2026, A&A, 707, A391
Stark, A. A. 1977, ApJ, 213, 368
Tacchella, S., Dekel, A., Carollo, C. M., et al. 2016, MNRAS, 458, 242
Tomassetti, M., Dekel, A., Mandelker, N., et al. 2016, MNRAS, 458, 4477
Tremblay, B. & Merritt, D. 1995, AJ, 110, 1039
van de Ven, G. & van der Wel, A. 2021, ApJ, 914, 45
van Der Wel, A., Bell, E. F., Häussler, B., et al. 2012, ApJS, 203, 24
van der Wel, A., Chang, Y.-Y., Bell, E. F., et al. 2014a, ApJ, 792, L6
van der Wel, A., Franx, M., Van Dokkum, P. G., et al. 2014b, ApJ, 788, 28
Van Dokkum, P. G., Nelson, E. J., Franx, M., et al. 2015, ApJ, 813, 23
Vats, D., Flegal, J. M., & Jones, G. L. 2019, Biometrika, 106, 321
Vehtari, A., Gelman, A., Simpson, D., Carpenter, B., & Bürkner, P.-C. 2021, Bayesian Anal., 16, 667
Vincent, R. A. & Ryden, B. S. 2005, ApJ, 623, 137
Walmsley, M., Allen, C., Aussel, B., et al. 2023, JOSS, 8, 5312
Yang, L., Kartaltepe, J. S., Drakos, N. E., et al. 2026, arXiv:2606.14869
Yuma, S., Ohta, K., & Yabe, K. 2012, ApJ, 761, 19
Zhang, H., Primack, J. R., Faber, S. M., et al. 2019, MNRAS, 484, 5170
Zhang, J., Wuyts, S., Cutler, S. E., et al. 2023, MNRAS, 524, 4128
Zhang, J., Wuyts, S., Witten, C., et al. 2022, MNRAS, 513, 4814
Zolotov, A., Dekel, A., Mandelker, N., et al. 2015, MNRAS, 450, 2327

Authors and affiliations

M. Dunn[⋆1,2,3], M. Huertas-Company[1,4,5], J. H. Knapen[1,2], V. Pandya[6], H. Zhang[7], L. Quilley[8], A. van der Wel[9], E. Duran-Camacho[1,2], D. Scott[10], G. Helou[11], K. Bunte[3], B. Altieri[12], S. Andreon[13], N. Auricchio[14], C. Baccigalupi[15,16,17,18], M. Baldi[19,14,20], S. Bardelli[14], P. Battaglia[14], A. Biviano[16,15], E. Branchini[21,22,13], M. Brescia[23,24], S. Camera[25,26,27], V. Capobianco[27], C. Carbone[28], J. Carretero[29,30], M. Castellano[31], G. Castignani[14], S. Cavuoti[24,32], K. C. Chambers[33], A. Cimatti[34], C. Colodro-Conde[1], G. Congedo[35], C. J. Conselice[8], L. Conversi[36,12], Y. Copin[37], F. Courbin[38,39,40], H. M. Courtois[41], M. Cropper[42], H. Degaudenzi[43], G. De Lucia[16], C. Dolding[42], H. Dole[44], F. Dubath[43], X. Dupac[12], S. Dusini[45], A. Ealet[37], S. Escoffier[46], M. Farina[47], R. Farinelli[14], S. Ferriol[37], P. Fosalba[48,49], S. Fotopoulou[50], M. Frailis[16], E. Franceschi[14], M. Fumana[28], S. Galeotta[16], K. George[51], B. Gillis[35], C. Giocoli[14,20], J. Gracia-Carpio[52], A. Grazian[53], F. Grupp[52,54], S. Gwyn[55], S. V. H. Haugan[56], W. Holmes[57], F. Hormuth[58], A. Hornstrup[59,60], K. Jahnke[61], M. Jhabvala[62], B. Joachimi[63], S. Kermiche[46], A. Kiessling[57], B. Kubik[37], M. Kümmel[54], H. Kurki-Suonio[64,65], A. M. C. Le Brun[66], S. Ligori[27], P. B. Lilje[56], V. Lindholm[64,65], I. Lloro[67], M. Magliocchetti[47], G. Mainetti[68], O. Mansutti[16], O. Marggraf[69], M. Martinelli[31,70], N. Martinet[71], F. Marulli[72,14,20], R. J. Massey[73], E. Medinaceli[14], S. Mei[74,75], M. Melchior[76], M. Meneghetti[14,20], E. Merlin[53], G. Meylan[77], A. Mora[78], M. Moresco[72,14], C. Moretti[16,15,17], L. Moscardini[72,14,20], R. Nakajima[69], C. Neissner[79,30], S.-M. Niemi[80], J. W. Nightingale[81], C. Padilla[79], S. Paltani[43], F. Pasian[16], K. Pedersen[82], W. J. Percival[83,84,85], V. Pettorino[80], A. Pezzotta[13], G. Polenta[86], M. Poncet[87], L. A. Popa[88], L. Pozzetti[14], F. Raison[52], A. Renzi[89,45,14], J. Rhodes[57], G. Riccio[24], E. Romelli[16], M. Roncarelli[14], B. Rusholme[90], R. Saglia[54,52], Z. Sakr[91,92,93], D. Sapone[94], B. Sartoris[54,16], P. Schneider[69], T. Schrabback[95], M. Scodeggio[28], A. Secroun[46], E. Sihvola[96], P. Simon[69], C. Sirignano[89,45], G. Sirri[20], L. Stanco[45], P. Tallada-Crespí[29,30], A. N. Taylor[35], H. I. Teplitz[97], I. Tereno[98,99], N. Tessore[42], S. Toft[100,101], R. Toledo-Moreo[102,103], F. Torradeflot[30,29], I. Tutusaus[49,48,92], J. Valiviita[64,65], T. Vassallo[16,51], A. Veropalumbo[13,22,21], Y. Wang[90], J. Weller[54,52], A. Zacchei[16,15], G. Zamorani[14], F. M. Zerbi[13], I. A. Zinchenko[104], E. Zucca[14], and M. Sereno[14,20]

[1] Instituto de Astrofísica de Canarias, E-38205 La Laguna, Tenerife, Spain
[2] Universidad de La Laguna, Dpto. Astrofísica, E-38206 La Laguna, Tenerife, Spain
[3] Bernoulli Institute for Mathematics, Computer Science and Artificial Intelligence, University of Groningen, PO Box 407, 9700 AK Groningen, The Netherlands
[4] Université PSL, Observatoire de Paris, Sorbonne Université, CNRS, LERMA, 75014, Paris, France
[5] Université Paris-Cité, 5 Rue Thomas Mann, 75013, Paris, France
[6] Columbia Astrophysics Laboratory, Columbia University, 550 West 120th Street, New York, NY 10027, USA
[7] Canadian Institute for Theoretical Astrophysics, Toronto, ON M5S 3H8, Canada
[8] Jodrell Bank Centre for Astrophysics, Department of Physics and Astronomy, University of Manchester, Oxford Road, Manchester M13 9PL, UK
[9] Universiteit Gent, Department of Physics and Astronomy, Proeftuinstraat 86 N3, 9000 Ghent, Belgium
[10] Department of Physics and Astronomy, University of British Columbia, Vancouver, BC V6T 1Z1, Canada
[11] California Institute of Technology, 1200 E California Blvd, Pasadena, CA 91125, USA
[12] ESAC/ESA, Camino Bajo del Castillo, s/n., Urb. Villafranca del Castillo, 28692 Villanueva de la Cañada, Madrid, Spain
[13] INAF-Osservatorio Astronomico di Brera, Via Brera 28, 20122 Milano, Italy
[14] INAF-Osservatorio di Astrofisica e Scienza dello Spazio di Bologna, Via Piero Gobetti 93/3, 40129 Bologna, Italy
[15] IFPU, Institute for Fundamental Physics of the Universe, via Beirut 2, 34151 Trieste, Italy
[16] INAF-Osservatorio Astronomico di Trieste, Via G. B. Tiepolo 11, 34143 Trieste, Italy
[17] INFN, Sezione di Trieste, Via Valerio 2, 34127 Trieste TS, Italy
[18] SISSA, International School for Advanced Studies, Via Bonomea 265, 34136 Trieste TS, Italy
[19] Dipartimento di Fisica e Astronomia, Università di Bologna, Via Gobetti 93/2, 40129 Bologna, Italy
[20] INFN-Sezione di Bologna, Viale Berti Pichat 6/2, 40127 Bologna, Italy
[21] Dipartimento di Fisica, Università di Genova, Via Dodecaneso 33, 16146, Genova, Italy
[22] INFN-Sezione di Genova, Via Dodecaneso 33, 16146, Genova, Italy
[23] Department of Physics "E. Pancini", University Federico II, Via Cinthia 6, 80126, Napoli, Italy
[24] INAF-Osservatorio Astronomico di Capodimonte, Via Moiariello 16, 80131 Napoli, Italy
[25] Dipartimento di Fisica, Università degli Studi di Torino, Via P. Giuria 1, 10125 Torino, Italy
[26] INFN-Sezione di Torino, Via P. Giuria 1, 10125 Torino, Italy
[27] INAF-Osservatorio Astrofisico di Torino, Via Osservatorio 20, 10025 Pino Torinese (TO), Italy
[28] INAF-IASF Milano, Via Alfonso Corti 12, 20133 Milano, Italy
[29] Centro de Investigaciones Energéticas, Medioambientales y Tecnológicas (CIEMAT), Avenida Complutense 40, 28040 Madrid, Spain
[30] Port d'Informació Científica, Campus UAB, C. Albareda s/n, 08193 Bellaterra (Barcelona), Spain
[31] INAF-Osservatorio Astronomico di Roma, Via Frascati 33, 00078 Monteporzio Catone, Italy
[32] INFN – Sezione di Napoli, Via Cinthia 6, 80126, Napoli, Italy
[33] Institute for Astronomy, University of Hawaii, 2680 Woodlawn Drive, Honolulu, HI 96822, USA
[34] Dipartimento di Fisica e Astronomia "Augusto Righi" - Alma Mater Studiorum Università di Bologna, Viale Berti Pichat 6/2, 40127 Bologna, Italy

[35] Institute for Astronomy, University of Edinburgh, Royal Observatory, Blackford Hill, Edinburgh EH9 3HJ, UK
[36] European Space Agency/ESRIN, Largo Galileo Galilei 1, 00044 Frascati, Roma, Italy
[37] Université Claude Bernard Lyon 1, CNRS/IN2P3, IP2I Lyon, UMR 5822, Villeurbanne, F-69100, France
[38] Institut de Ciències del Cosmos (ICCUB), Universitat de Barcelona (IEEC-UB), Martí i Franquès 1, 08028 Barcelona, Spain
[39] Institució Catalana de Recerca i Estudis Avançats (ICREA), Passeig de Lluís Companys 23, 08010 Barcelona, Spain
[40] Institut de Ciencies de l'Espai (IEEC-CSIC), Campus UAB, Carrer de Can Magrans, s/n Cerdanyola del Vallés, 08193 Barcelona, Spain
[41] UCB Lyon 1, CNRS/IN2P3, IUF, IP2I Lyon, 4 rue Enrico Fermi, 69622 Villeurbanne, France
[42] Mullard Space Science Laboratory, University College London, Holmbury St Mary, Dorking, Surrey RH5 6NT, UK
[43] Department of Astronomy, University of Geneva, ch. d'Ecogia 16, 1290 Versoix, Switzerland
[44] Université Paris-Saclay, CNRS, Institut d'astrophysique spatiale, 91405, Orsay, France
[45] INFN-Padova, Via Marzolo 8, 35131 Padova, Italy
[46] Aix-Marseille Université, CNRS/IN2P3, CPPM, Marseille, France
[47] INAF-Istituto di Astrofisica e Planetologia Spaziali, via del Fosso del Cavaliere, 100, 00100 Roma, Italy
[48] Institut d'Estudis Espacials de Catalunya (IEEC), Edifici RDIT, Campus UPC, 08860 Castelldefels, Barcelona, Spain
[49] Institute of Space Sciences (ICE, CSIC), Campus UAB, Carrer de Can Magrans, s/n, 08193 Barcelona, Spain
[50] School of Physics, HH Wills Physics Laboratory, University of Bristol, Tyndall Avenue, Bristol, BS8 1TL, UK
[51] University Observatory, LMU Faculty of Physics, Scheinerstr. 1, 81679 Munich, Germany
[52] Max Planck Institute for Extraterrestrial Physics, Giessenbachstr. 1, 85748 Garching, Germany
[53] INAF-Osservatorio Astronomico di Padova, Via dell'Osservatorio 5, 35122 Padova, Italy
[54] Universitäts-Sternwarte München, Fakultät für Physik, Ludwig-Maximilians-Universität München, Scheinerstr. 1, 81679 München, Germany
[55] National Research Council, Herzberg Astronomy and Astrophysics Research Centre, 5071 W. Saanich Rd. Victoria, BC, V9E 2E7, Canada
[56] Institute of Theoretical Astrophysics, University of Oslo, P.O. Box 1029 Blindern, 0315 Oslo, Norway
[57] Jet Propulsion Laboratory, California Institute of Technology, 4800 Oak Grove Drive, Pasadena, CA, 91109, USA
[58] Felix Hormuth Engineering, Goethestr. 17, 69181 Leimen, Germany
[59] Technical University of Denmark, Elektrovej 327, 2800 Kgs. Lyngby, Denmark
[60] Cosmic Dawn Center (DAWN), Denmark
[61] Max-Planck-Institut für Astronomie, Königstuhl 17, 69117 Heidelberg, Germany
[62] NASA Goddard Space Flight Center, Greenbelt, MD 20771, USA
[63] Department of Physics and Astronomy, University College London, Gower Street, London WC1E 6BT, UK
[64] Department of Physics, P.O. Box 64, University of Helsinki, 00014 Helsinki, Finland
[65] Helsinki Institute of Physics, Gustaf Hällströmin katu 2, University of Helsinki, 00014 Helsinki, Finland
[66] Laboratoire d'etude de l'Univers et des phenomenes eXtremes, Observatoire de Paris, Université PSL, Sorbonne Université, CNRS, 92190 Meudon, France
[67] SKAO, Jodrell Bank, Lower Withington, Macclesfield SK11 9FT, UK
[68] Centre de Calcul de l'IN2P3/CNRS, 21 avenue Pierre de Coubertin 69627 Villeurbanne Cedex, France
[69] Universität Bonn, Argelander-Institut für Astronomie, Auf dem Hügel 71, 53121 Bonn, Germany
[70] INFN-Sezione di Roma, Piazzale Aldo Moro, 2 - c/o Dipartimento di Fisica, Edificio G. Marconi, 00185 Roma, Italy
[71] Aix-Marseille Université, CNRS, CNES, LAM, Marseille, France
[72] Dipartimento di Fisica e Astronomia "Augusto Righi" - Alma Mater Studiorum Università di Bologna, via Piero Gobetti 93/2, 40129 Bologna, Italy
[73] Department of Physics, Institute for Computational Cosmology, Durham University, South Road, Durham, DH1 3LE, UK
[74] Université Paris Cité, CNRS, Astroparticule et Cosmologie, 75013 Paris, France
[75] CNRS-UCB International Research Laboratory, Centre Pierre Binétruy, IRL2007, CPB-IN2P3, Berkeley, USA
[76] University of Applied Sciences and Arts of Northwestern Switzerland, School of Engineering, 5210 Windisch, Switzerland
[77] Institute of Physics, Laboratory of Astrophysics, Ecole Polytechnique Fédérale de Lausanne (EPFL), Observatoire de Sauverny, 1290 Versoix, Switzerland
[78] Telespazio UK S.L. for European Space Agency (ESA), Camino bajo del Castillo, s/n, Urbanizacion Villafranca del Castillo, Villanueva de la Cañada, 28692 Madrid, Spain
[79] Institut de Física d'Altes Energies (IFAE), The Barcelona Institute of Science and Technology, Campus UAB, 08193 Bellaterra (Barcelona), Spain
[80] European Space Agency/ESTEC, Keplerlaan 1, 2201 AZ Noordwijk, The Netherlands
[81] School of Mathematics, Statistics and Physics, Newcastle University, Herschel Building, Newcastle-upon-Tyne, NE1 7RU, UK
[82] DARK, Niels Bohr Institute, University of Copenhagen, Jagtvej 155, 2200 Copenhagen, Denmark
[83] Waterloo Centre for Astrophysics, University of Waterloo, Waterloo, Ontario N2L 3G1, Canada
[84] Department of Physics and Astronomy, University of Waterloo, Waterloo, Ontario N2L 3G1, Canada
[85] Perimeter Institute for Theoretical Physics, Waterloo, Ontario N2L 2Y5, Canada
[86] Space Science Data Center, Italian Space Agency, via del Politecnico snc, 00133 Roma, Italy
[87] Centre National d'Etudes Spatiales – Centre spatial de Toulouse, 18 avenue Edouard Belin, 31401 Toulouse Cedex 9, France
[88] Institute of Space Science, Str. Atomistilor, nr. 409 Măgurele, Ilfov, 077125, Romania
[89] Dipartimento di Fisica e Astronomia "G. Galilei", Università di Padova, Via Marzolo 8, 35131 Padova, Italy
[90] Caltech/IPAC, 1200 E. California Blvd., Pasadena, CA 91125, USA
[91] Instituto de Física Teórica UAM-CSIC, Campus de Cantoblanco, 28049 Madrid, Spain
[92] Institut de Recherche en Astrophysique et Planétologie (IRAP), Université de Toulouse, CNRS, UPS, CNES, 14 Av. Edouard Belin, 31400 Toulouse, France
[93] Université St Joseph; Faculty of Sciences, Beirut, Lebanon
[94] Departamento de Física, FCFM, Universidad de Chile, Blanco Encalada 2008, Santiago, Chile
[95] Universität Innsbruck, Institut für Astro- und Teilchenphysik, Technikerstr. 25/8, 6020 Innsbruck, Austria
[96] Department of Physics and Helsinki Institute of Physics, Gustaf Hällströmin katu 2, University of Helsinki, 00014 Helsinki, Finland
[97] Infrared Processing and Analysis Center, California Institute of Technology, Pasadena, CA 91125, USA
[98] Departamento de Física, Faculdade de Ciências, Universidade de Lisboa, Edifício C8, Campo Grande, PT1749-016 Lisboa, Portugal

[99] Instituto de Astrofísica e Ciências do Espaço, Faculdade de Ciências, Universidade de Lisboa, Tapada da Ajuda, 1349-018 Lisboa, Portugal
[100] Cosmic Dawn Center (DAWN)
[101] Niels Bohr Institute, University of Copenhagen, Jagtvej 128, 2200 Copenhagen, Denmark
[102] Universidad Politécnica de Cartagena, Departamento de Electrónica y Tecnología de Computadoras, Plaza del Hospital 1, 30202 Cartagena, Spain
[103] European University of Technology EUt+, European Union
[104] Astronomisches Rechen-Institut, Zentrum für Astronomie der Universität Heidelberg, Mönchhofstr. 12-14, 69120 Heidelberg, Germany

⋆ e-mail: marina.dunn@iac.es

Appendix A: DR1 selection cuts

We use the following selections to build our magnitude-limited sample from the DR1 catalogue:

- $I_E \leq 24.5$, implemented by making a cut in the sum of the flux in the segmented pixels `FLUX_SEGMENTATION` $\gtrsim 0.575$;
- `VIS_DET` = 1 to ensure sources are detected in VIS mosaic tiles;
- `SPURIOUS_FLAGS` = 0 to prevent spurious sources from contaminating the sample;
- `POINT_LIKE_PROB` ≤ 0.1 to discard point-like sources;
- `PHYS_PARAM_FLAGS` = 0 indicating good physical parameter processing from the `PHZ` processing function;
- `PHZ_CLASSIFICATION` = 2, indicating the source is accepted as a galaxy by the `PHZ` processing function;
- `DET_QUALITY_FLAG` < 4 to remove poor-quality detections;
- `MUMAX_MINUS_MAG` > −2.6 to remove extended sources.

We then apply quality cuts, including those recommended by Euclid Collaboration: Quilley et al. (2026) and Euclid Collaboration: Enia et al. (in prep., their section 3), to our star-forming sample to ensure reliable measurements and physical parameters:

- |`PHZ_PP_MEDIAN_Z` − `PHZ_MEDIAN`| < 0.2;
- |`PHZ_PP_MEDIAN_Z` − `PHZ_PP_MODE_Z`| < 0.2;
- $0.01a$ < `SERSIC_SERSIC_VIS_RADIUS` < $20a$, where a in this case is the isophotal semi-major axis in units of VIS pixels;
- 0.302 < `SERSIC_SERSIC_VIS_INDEX` < 5.45 to limit the bounds of Sérsic indices;
- 0.05 < `SERSIC_SERSIC_VIS_AXIS_RATIO` < 1.0 to limit the bounds of Sérsic axis ratios;
- `SERSIC_SERSIC_VIS_AXIS_RATIO_ERR` < 0.10 to exclude sources with large errors in Sérsic axis ratio;
- `SERSIC_SERSIC_VIS_RADIUS_ERR` < 0.10 to exclude sources with large errors in angular Sérsic effective radius;
- `SERSIC_SERSIC_VIS_RADIUS` > 0.″16 to ensure angular Sérsic effective radii are larger than the VIS PSF FWHM;
- Finite values for `SERSIC_SERSIC_VIS_RADIUS`, `SERSIC_SERSIC_VIS_AXIS_RATIO`, `PHZ_PP_MEDIAN_STELLARMASS`, `PHZ_PP_MEDIAN_SFR`, and `PHZ_PP_MEDIAN_REDSHIFT`.

Appendix B: Sérsic parameter comparison

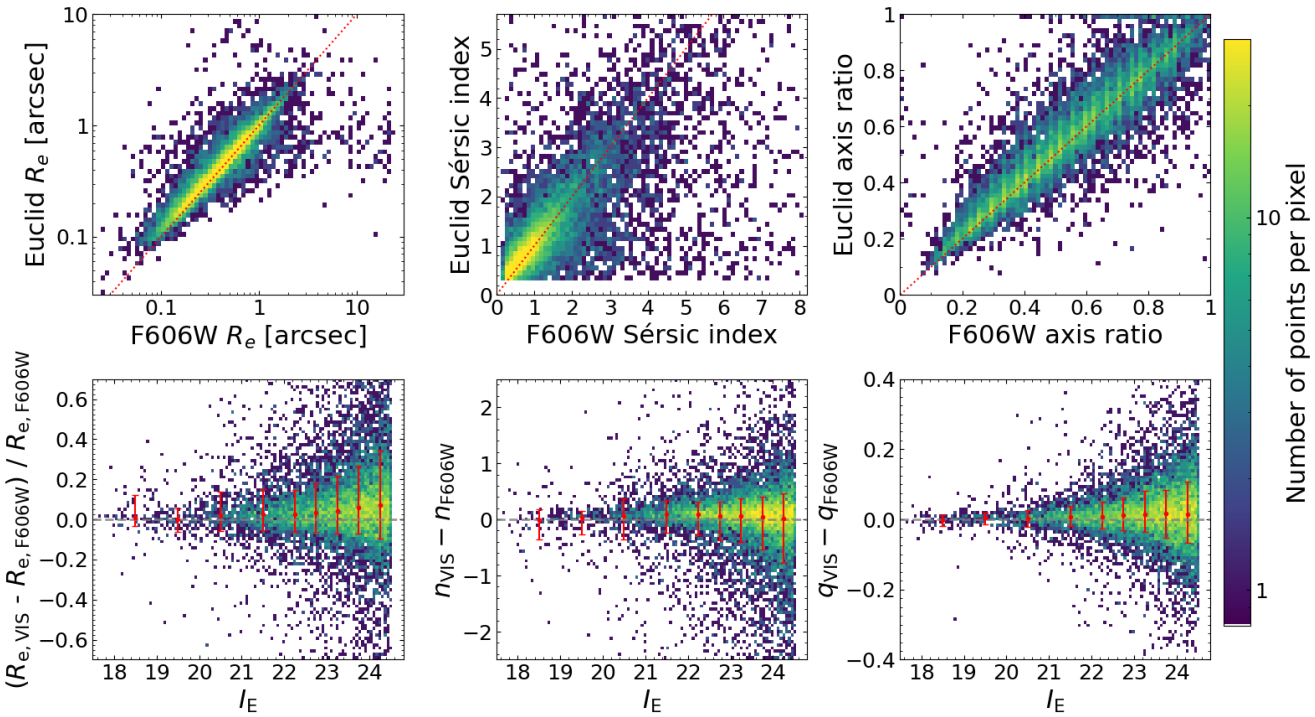


Fig. B.1. Comparison of Sérsic parameters for cross-matched galaxies with $I_E \leq 24.5$ between ACS-GC using HST F606W imaging, and single-visit DR1 EDF-F measurements at EWS depth. *Top row*: direct comparison of effective radius R_e (in arcseconds), Sérsic index n, and axis ratio q. *Bottom row*: differences (or relative differences) in each parameter as a function of I_E. Red points show the median per magnitude bin; error bars show the 16th and 84th percentiles of the distribution.

Following Euclid Collaboration: Quilley et al. (2026, section 4), we compare Sérsic parameters for cross-matched galaxies with $I_E \leq 24.5$ in the GEMS field between the Advanced Camera for Surveys General Catalog (ACS-GC; Griffith et al. 2012), whose fits were performed with `GALAPAGOS` (Barden et al. 2012) on HST F606W images, and a single DR1 EDF-F visit at EWS depth (Fig. B.1). The top row compares Sérsic parameters (effective radius R_e, in arcseconds; index n; and axis ratio q) between *Euclid* and ACS-GC, while the bottom row shows the difference (or relative difference) for each parameter as a function of magnitude (based

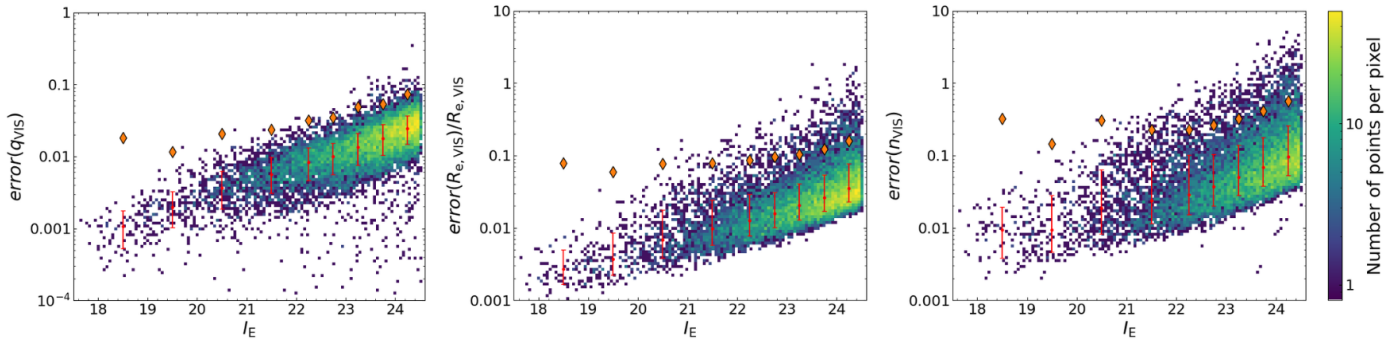


Fig. B.2. Uncertainties in q, R_e, and n as a function of I_E for the same cross-matched sample as in Fig. B.1. Red points and error bars show the median, and 16th/84th percentiles per magnitude bin. Orange diamonds show dispersion of differences between *Euclid* and ACS-GC from Fig. B.1.

on MER `FLUX_SEGMENTATION`), with red points indicating the median, and error bars indicating the 16th and 84th percentiles of the distribution, per magnitude bin.

Figure B.2 shows how the measured errors for q, R_e, and n vary with magnitude, again with the per-bin median, 16th, and 84th percentiles in red; the orange diamonds indicate the dispersion around the median, defined as the 68th percentile of $|y - \mathrm{median}(y)|$. The different bandpasses in HST and *Euclid* introduce systematic offsets between the two data sets, so ACS-GC measurements do not constitute a perfect 'ground truth' for this comparison. This bandpass mismatch also contributes to the dispersion itself: galaxies with different colour gradients suffer different biases, adding scatter beyond the purely statistical measurement uncertainty. Quantitatively, the dispersion for R_e increases steadily towards fainter magnitudes, rising from $\lesssim 10\%$ at $I_E < 23$ to $\sim 16\%$ in the bin $24.0 < I_E < 24.5$, while for q it remains smaller throughout, increasing from $\lesssim 3\%$ to $\sim 7\%$. The corresponding systematic offsets are modest, with R_e biased high by $\sim 7\%$ and q by $\lesssim 2\%$ at the faint limit. Sérsic index n is by far the least well constrained of the three parameters, with a dispersion several times larger than that of R_e or q ($D \sim 0.57$ by $I_E = 24.5$). These trends closely follow those found for the comparison between Q1 and ACS-GC in Euclid Collaboration: Quilley et al. (2026, figure 6). We note that the DR1 sample Sérsic parameter error selection cut (Appendix A) only applies to Sérsic q and R_e, not Sérsic n.

We also compare the single-Sérsic structural parameters of our final sample with the isophotal-based measurements ($a_{\rm iso}$ = `SEMIMAJOR_AXIS`, $q_{\rm iso} = 1 - $ `ELLIPTICITY`) in the MER catalogue. We convert $a_{\rm iso}$ from pixels to arcseconds. These measurements are not PSF-corrected, whereas the Sérsic parameters come from PSF-convolved model fits and are therefore corrected for the PSF. Medians and scatters are computed over all galaxies with both $a_{\rm iso}$ and $a_{\rm Sérsic}$ larger than the VIS PSF FWHM, with the scatter defined as half the difference between the 16th and 84th percentiles of the distribution (equivalent to 1σ for a Gaussian distribution). The two size measures are tightly correlated (Fig. B.3, left) with a median $\log_{10}(a_{\rm Sérsic}/a_{\rm iso}) = 0.081$ and a scatter of 0.074 dex. Sérsic radii are slightly larger on average, as expected for two different definitions of size, and extend to smaller values because they are corrected for the PSF. The axis ratios (Fig. B.3, right) show a median offset $q_{\rm Sérsic} - q_{\rm iso} = -0.093$ with a scatter of 0.091, consistent with the Q1 result of Euclid Collaboration: Quilley et al. (2026), because the isophotal-based shapes are rounded by the PSF. Looking at the distributions of axis ratios as a function of Sérsic index, this offset is present at all Sérsic indices (Fig. B.4). As in Euclid Collaboration: Quilley et al. (2026, figures 2 and 3), pure disc galaxies with $n \sim 1$ span the full range of axis ratios, $0.1 \lesssim q \leq 1$, as expected for discs seen at all inclinations. The Sérsic axis ratios recover more of these discs at very low q, since PSF rounding prevents the isophotal-based measurements from reaching the axis ratios of thin, edge-on systems.

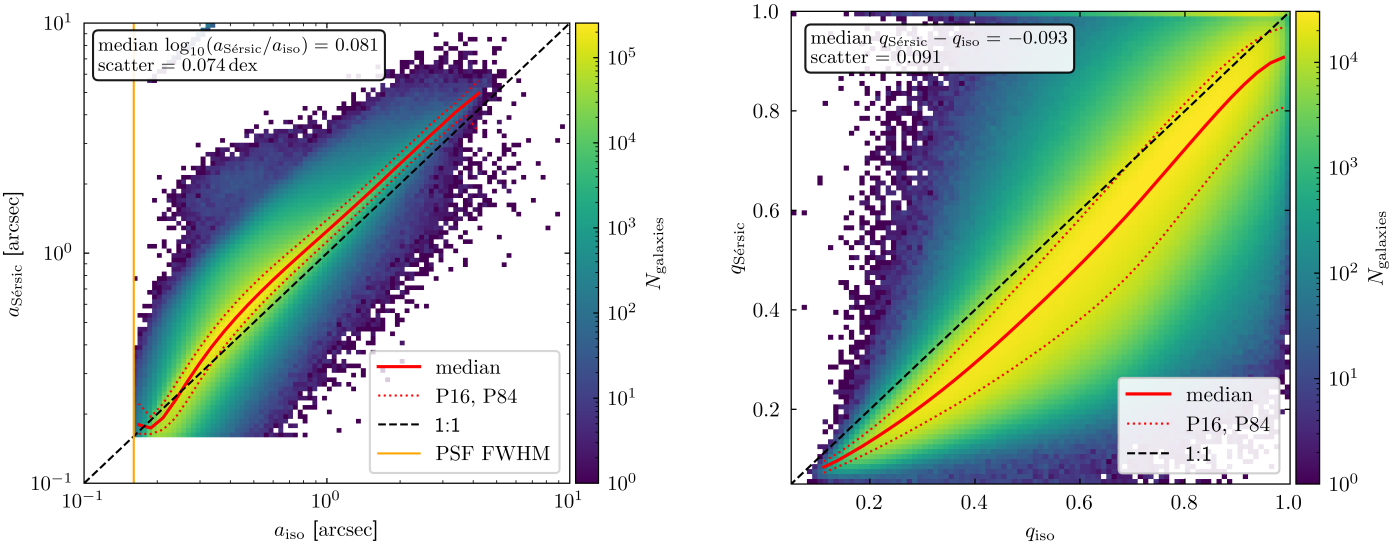


Fig. B.3. Comparison of single-Sérsic and isophotal-based structural parameters for our final sample with both $a_{\rm iso}$ and $a_{\rm Sérsic}$ larger than the VIS PSF FWHM (0.″16). *Left*: Sérsic effective radius $a_{\rm Sérsic}$ versus isophotal semi-major axis $a_{\rm iso}$, in arcseconds; the orange line marks the PSF FWHM. *Right*: Sérsic axis ratio $q_{\rm Sérsic}$ versus isophotal axis ratio $q_{\rm iso}$. Colours show the number of galaxies per pixel (logarithmic scale). Solid and dotted red lines show the running median, and the 16th and 84th percentiles in bins of the x-axis quantity. The dashed black line marks the 1:1 relation.

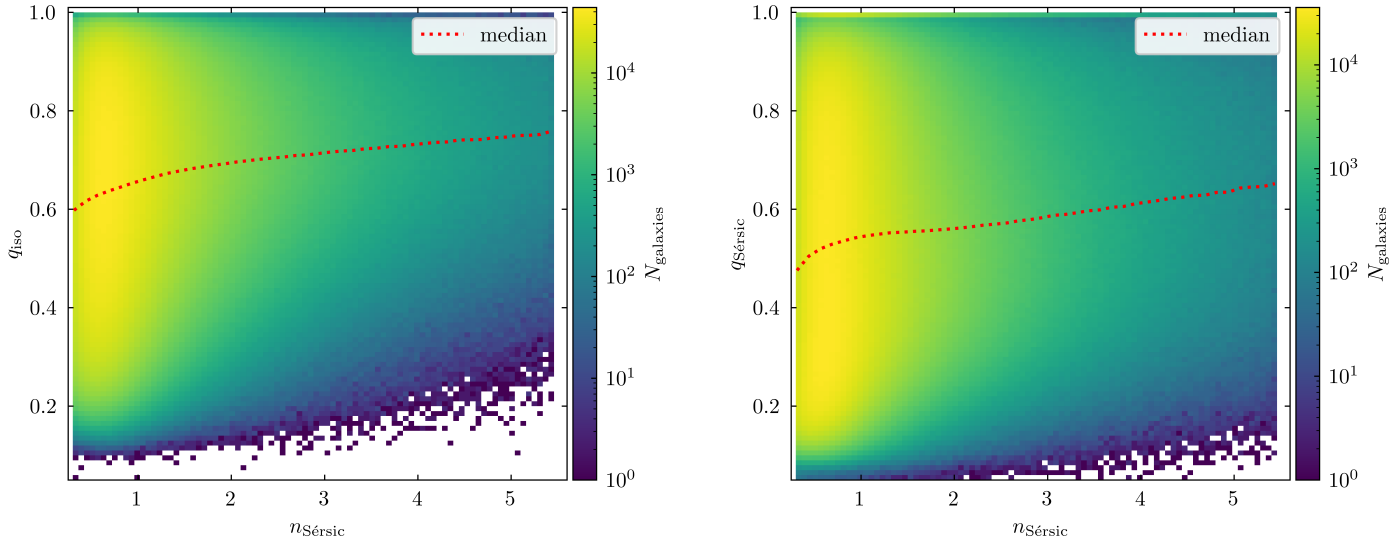


Fig. B.4. Axis ratio as a function of Sérsic index n for the same galaxies as Fig. B.3, using the isophotal axis ratio $q_{\rm iso}$ (*left*) and the Sérsic axis ratio $q_{\rm Sérsic}$ (*right*). Colours show the number of galaxies per pixel (logarithmic scale); dotted red lines show the running median q in bins of $\Delta n = 0.125$.

Appendix C: Star-forming galaxy selection

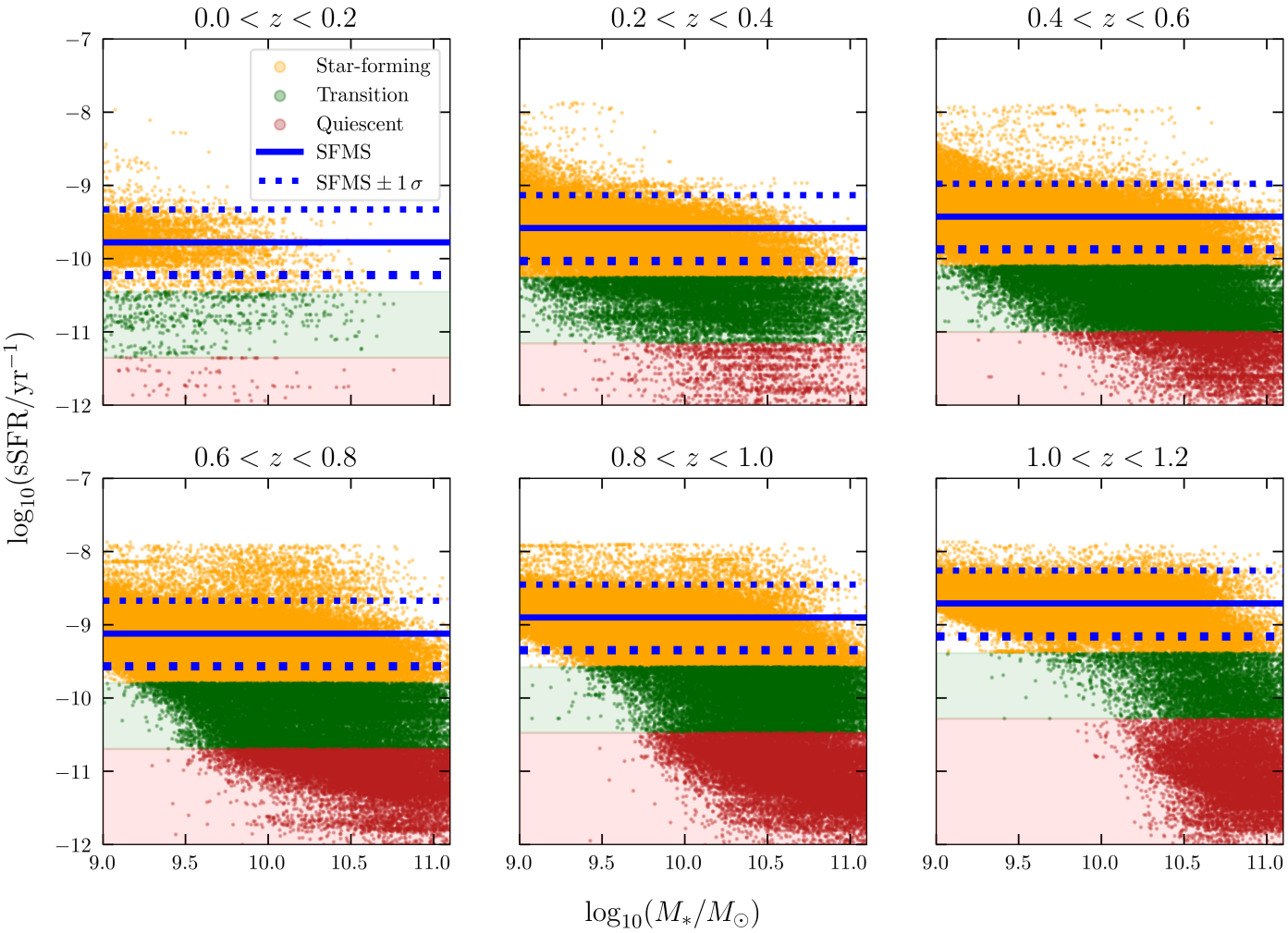


Fig. C.1. sSFR–M_* diagrams per redshift slice. The solid blue line indicates the sSFR of the zero-slope median SFMS; dotted blue lines indicate the 0.45 dex ($\pm 1\,\sigma$) width of the SFMS. Galaxies are classified as star-forming if they are located above the lower dotted blue line, transition if located in the green shaded region ($1.5\,\sigma$–$3.5\,\sigma$ below the SFMS), and quiescent if located in the red shaded region ($>\ 3.5\,\sigma$ below the SFMS).

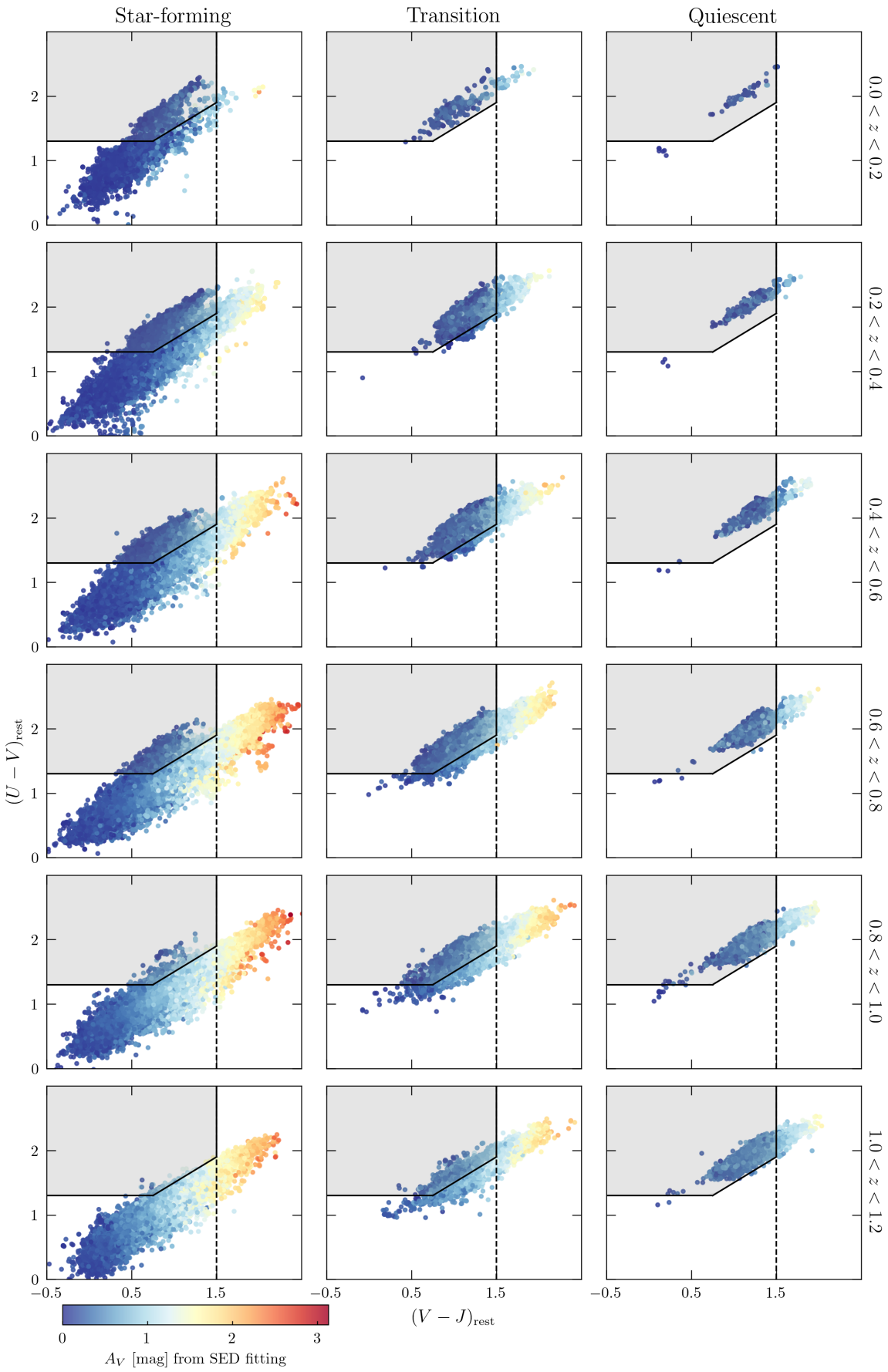


Fig. C.2. Rest-frame $(U - V)$ vs. $(V - J)$ diagrams for each redshift slice, divided into columns of star-forming, transition, and quiescent galaxy populations, and colour-coded by optical dust attenuation A_V from SED fitting by Euclid Collaboration: Enia et al. (in prep.). Quiescent wedges (shaded regions bounded by solid black lines) contain galaxies satisfying the relations in Eq. (3).

Appendix D: Mock HMC parameter recovery tests

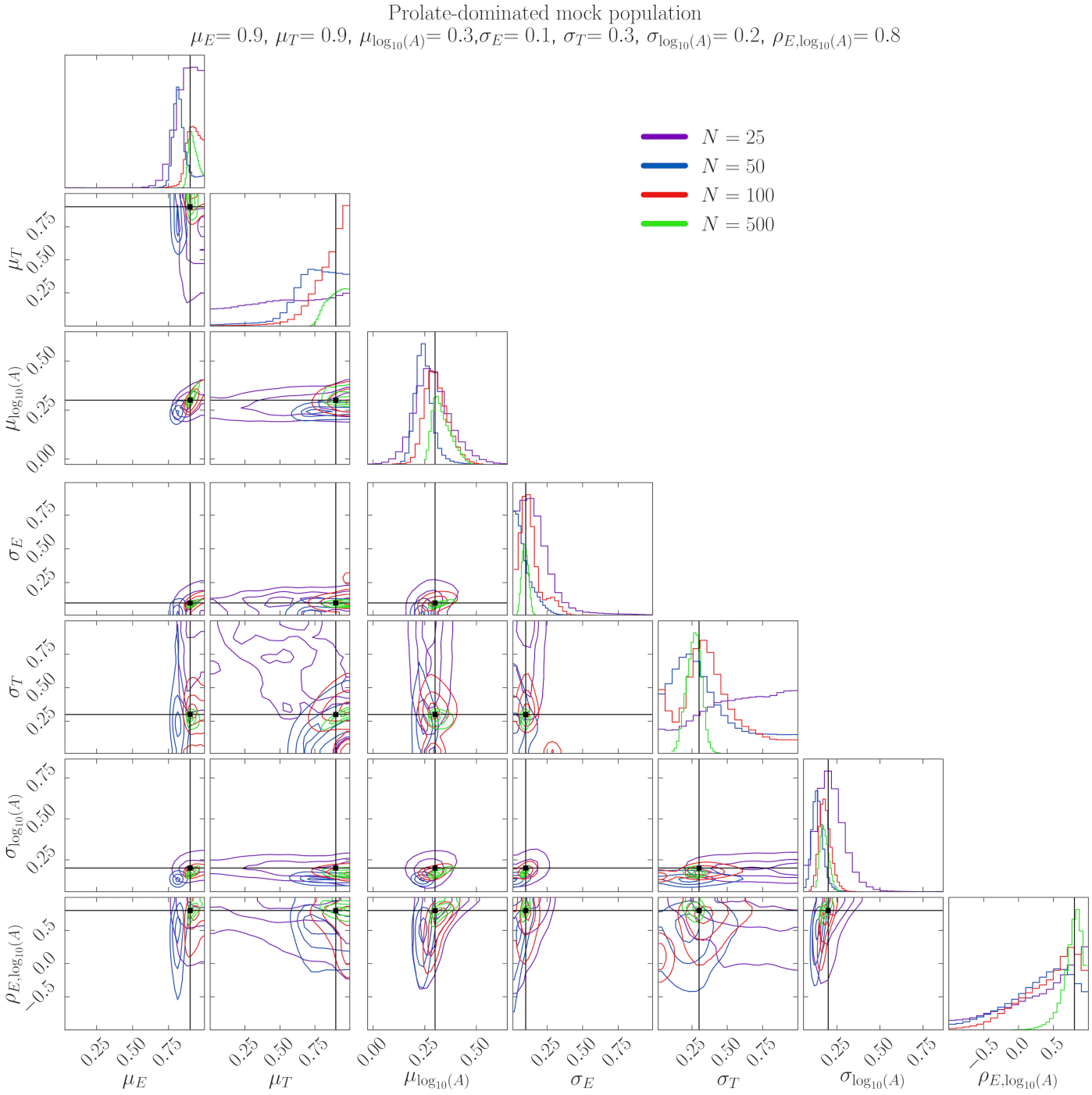


Fig. D.1. Corner plot (Foreman-Mackey 2016) showing HMC recovery of shape parameters for a prolate-dominated mock population with varying sample sizes: N = 500 (green); 100 (red); 50 (blue); and 25 (purple). Contours show the 11.8% (0.5 σ), 39.3% (1 σ), and 67.5% (1.5 σ) credible levels; black lines mark ground-truth values (listed in the title).

We perform mock parameter-recovery tests following the procedure of P24 to assess the robustness of our model and the HMC NUTS sampler. We generate synthetic galaxy populations corresponding to three intrinsic shape regimes by varying only the mean ellipticity and triaxiality: prolate-dominated ($\mu_E = 0.9, \mu_T = 0.9$), oblate-dominated ($\mu_E = 0.9, \mu_T = 0.1$), and spheroid-dominated ($\mu_E = 0.1, \mu_T = 0.1$). All other parameters are at fixed values; $\mu_{\log_{10}(A)} = 0.3$, $\sigma_E = 0.2$, $\sigma_T = 0.2$, $\sigma_{\log_{10}(A)} = 0.2$, and $\rho_{E,\log_{10}(A)} = 0.8$. For each shape class, we generate mock 2D b/a versus $\log_{10}(a)$ histograms with varying sample sizes ($N = 25, 50, 100, 500$) to study how the fidelity of posterior recovery scales with the number of observed galaxies. We then perform inference with `PyMC` using the same HMC sampling setup, and compare the inferred posterior means to the ground-truth parameter values. Figure D.1 shows a corner plot (Foreman-Mackey 2016) for a parameter recovery test for an example prolate-dominated mock ellipsoid population for different sample sizes (N = 500, 100, 50, and 25). As in P24, the HMC model can successfully recover the true parameters

for samples as small as $N = 50$, but struggles at lower sample sizes – particularly for μ_T and σ_T – making it difficult to reliably distinguish prolate from oblate populations.

Appendix E: Data sample completeness

We first evaluate the morphological completeness across the b/a–size plane for our sample using mock galaxies from the *Euclid* Morphology Challenge (Euclid Collaboration: Merlin et al. 2023; Euclid Collaboration: Bretonnière et al. 2023). For both the mock sources and our magnitude-limited sample, we use the axis ratios b/a and effective (half-light) radii (R_e, in arcseconds) from single-component Sérsic fits to VIS images with `SourceXtractor++`, and compare the two distributions to assess the detection fraction. Figure E.1 shows the detection fraction for three different bins of brightness: (1) 'bright' mock sources with $14.8 \leq I_E < 23$; (2) 'moderately faint' mock sources with $23 \leq I_E < 24.5$; and (3) 'very faint' mock sources with $24.5 \leq I_E < 26$. Crucially, across the magnitude range of our sample ($I_E \leq 24.5$), completeness remains high in the upper right of the b/a–size plane, where large face-on discs (high b/a, large R_e) reside. These are the objects most vulnerable to surface-brightness dimming and thus most likely to be lost from a magnitude-limited sample; their retention indicates that our inferred shape distributions are not strongly biased against intrinsically flat, extended systems. The most incomplete region is instead confined to faint, compact sources (low b/a, low R_e) beyond our magnitude limit, which contribute least to the population-level shape constraints.

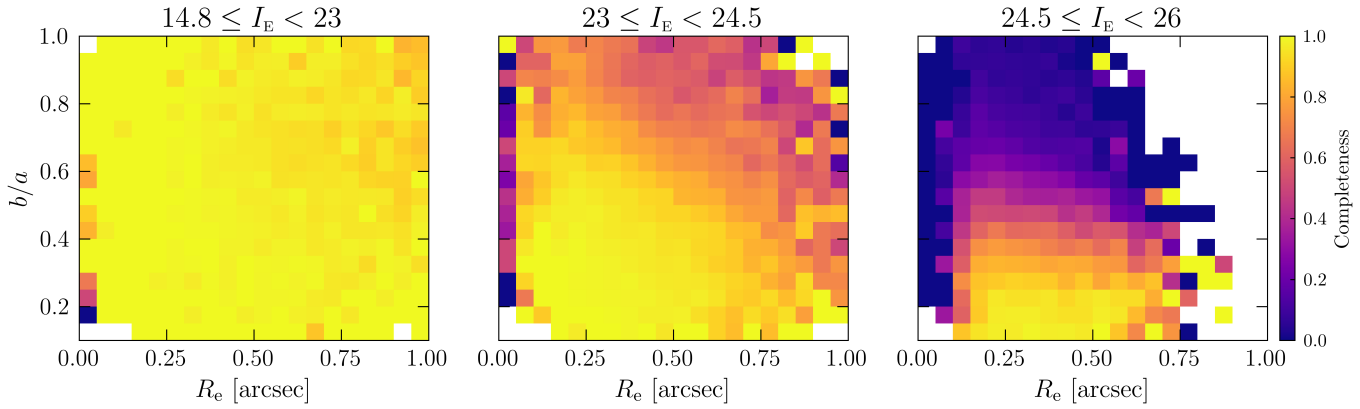


Fig. E.1. Detection fraction across the b/a–size plane based on mock single-Sérsic fits to VIS images from the *Euclid* Morphology Challenge. *Left*: mock galaxies with $14.8 \leq I_E < 23$; *Middle*: mock galaxies with $23 \leq I_E < 24.5$; *Right*: mock galaxies with $24.5 \leq I_E < 26$.

We also assess stellar mass completeness by applying the method of Pozzetti et al. (2010) to our DR1 magnitude-limited ($I_E \leq 24.5$) star-forming sample. We compute the stellar masses at which the sample reaches 95%, 90%, and 50% completeness, indicated by the black lines in Fig. E.2. We find that the sample is at least 90% complete for all bins except bins $\log_{10}(M_*/M_\odot) = 9.0$–$9.5$ at $0.8 < z < 1.0$ and $1.0 < z < 1.2$, which reach 75% and 50% completeness, respectively. Nevertheless, Fig. 2 shows that there is no significant increase in shape parameter uncertainties at higher redshifts. Given this, and the fact that our mock detection fraction remains nearly complete across the b/a–size plane, mass completeness should not strongly bias morphological classifications. We reiterate that future *Euclid* releases will push completeness limits to lower masses.

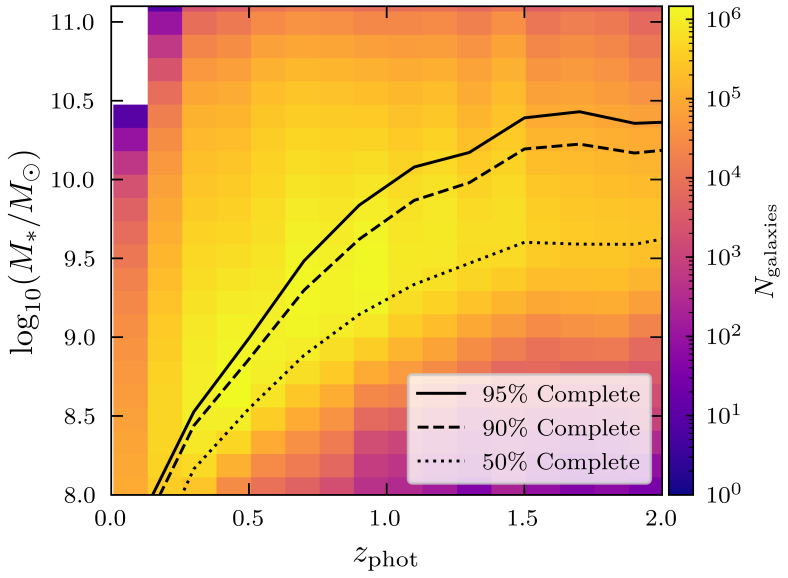


Fig. E.2. Mass completeness of the magnitude-limited sample; 95%, 90%, and 50% limits (black lines) are derived following Pozzetti et al. (2010).

Appendix F: 3D shape modelling results

Table F.1 provides basic convergence diagnostic statistics (described in Sect. 2) per bin from PyMC NUTS sampling across all chains. Table F.2 tabulates the results of our inference model from random draws of the posterior for each mass-redshift bin.

Table F.1. Convergence diagnostic statistics from NUTS sampling with PyMC for each mass-redshift bin from the posterior means. Statistics here include the minimum bulk effective sample size $\mathrm{ESS}_{\mathrm{bulk,\,min}}$, the minimum tail effective sample size $\mathrm{ESS}_{\mathrm{tail,\,min}}$, the maximum $\hat{R}_{\mathrm{max}}$, and the minimum BFMI, $\mathrm{BFMI}_{\mathrm{min}}$, across all sampling chains.

z	$\log_{10}(M_*/M_\odot)$	N_{galaxies}	$\hat{R}_{\mathrm{max}}$	$\mathrm{ESS}_{\mathrm{bulk,\,min}}$	$\mathrm{ESS}_{\mathrm{tail,\,min}}$	$\mathrm{BFMI}_{\mathrm{min}}$
0.0–0.2	9.0–9.5	306 909	1.003	1989.517	2581.169	1.017
0.0–0.2	9.5–10.0	109 780	1.001	4693.701	4701.812	0.961
0.0–0.2	10.0–10.5	21 000	1.001	4218.635	2996.148	0.940
0.2–0.4	9.0–9.5	2 694 631	1.002	2458.077	3020.175	0.978
0.2–0.4	9.5–10.0	1 462 850	1.002	3501.545	3608.021	0.975
0.2–0.4	10.0–10.5	694 841	1.001	5245.822	3371.312	0.964
0.4–0.6	9.0–9.5	3 983 560	1.001	5329.382	5143.545	1.012
0.4–0.6	9.5–10.0	2 386 934	1.001	5233.964	3805.091	0.992
0.4–0.6	10.0–10.5	1 313 521	1.002	4156.797	3748.746	0.972
0.6–0.8	9.0–9.5	4 717 101	1.001	5701.216	5447.162	1.014
0.6–0.8	9.5–10.0	3 779 549	1.004	5291.588	5156.641	1.020
0.6–0.8	10.0–10.5	1 898 979	1.002	3872.312	5028.314	0.992
0.8–1.0	9.0–9.5	4 362 066	1.001	5299.914	5526.251	1.009
0.8–1.0	9.5–10.0	4 416 628	1.001	4867.143	5254.788	0.981
0.8–1.0	10.0–10.5	2 067 640	1.002	4025.050	4910.138	0.987
1.0–1.2	9.0–9.5	1 875 729	1.001	5368.448	5253.693	1.027
1.0–1.2	9.5–10.0	2 961 898	1.001	5288.332	5132.424	1.031
1.0–1.2	10.0–10.5	1 480 278	1.002	1965.738	2535.839	1.032

Table F.2. Mean and standard deviations for the inferred seven 3D shape parameters and class fractions in each mass-redshift bin from random draws from the posterior. Uncertainties are statistical only.

z	$\log_{10}(M_*/M_\odot)$	$N_{\rm galaxies}$	μ_E	μ_T	$\mu_{\log_{10}(A)}$	σ_E	σ_T	$\sigma_{\log_{10}(A)}$	$\rho_{E,\log_{10}(A)}$	$f_{\rm prolate}$	$f_{\rm oblate}$	$f_{\rm spheroid}$
0.0–0.2	9.0–9.5	306 909	0.809 ± 0.002	0.275 ± 0.004	0.584 ± 0.002	0.177 ± 0.001	0.196 ± 0.004	0.250 ± 0.001	0.854 ± 0.002	0.043 ± 0.002	0.763 ± 0.003	0.194 ± 0.002
0.0–0.2	9.5–10.0	109 780	0.806 ± 0.001	0.168 ± 0.011	0.652 ± 0.001	0.088 ± 0.002	0.180 ± 0.009	0.226 ± 0.001	0.875 ± 0.003	0.011 ± 0.002	0.965 ± 0.003	0.024 ± 0.002
0.0–0.2	10.0–10.5	21 000	0.821 ± 0.001	0.008 ± 0.008	0.769 ± 0.002	0.059 ± 0.002	0.386 ± 0.016	0.169 ± 0.002	0.873 ± 0.009	0.113 ± 0.012	0.884 ± 0.012	0.003 ± 0.001
0.2–0.4	9.0–9.5	2 694 631	0.797 ± 0.000	0.277 ± 0.002	0.544 ± 0.000	0.130 ± 0.000	0.229 ± 0.001	0.236 ± 0.000	0.884 ± 0.001	0.080 ± 0.001	0.798 ± 0.001	0.122 ± 0.000
0.2–0.4	9.5–10.0	1 462 850	0.781 ± 0.000	0.108 ± 0.006	0.614 ± 0.000	0.117 ± 0.001	0.223 ± 0.004	0.221 ± 0.000	0.887 ± 0.001	0.019 ± 0.001	0.885 ± 0.001	0.096 ± 0.001
0.2–0.4	10.0–10.5	694 841	0.781 ± 0.000	0.001 ± 0.001	0.722 ± 0.000	0.086 ± 0.000	0.336 ± 0.002	0.187 ± 0.000	0.870 ± 0.001	0.073 ± 0.002	0.879 ± 0.002	0.048 ± 0.001
0.4–0.6	9.0–9.5	3 983 560	0.791 ± 0.000	0.341 ± 0.001	0.544 ± 0.000	0.093 ± 0.000	0.269 ± 0.001	0.208 ± 0.000	0.838 ± 0.001	0.177 ± 0.001	0.760 ± 0.001	0.063 ± 0.000
0.4–0.6	9.5–10.0	2 386 934	0.782 ± 0.000	0.000 ± 0.000	0.631 ± 0.000	0.086 ± 0.000	0.460 ± 0.001	0.205 ± 0.000	0.888 ± 0.001	0.166 ± 0.001	0.783 ± 0.001	0.050 ± 0.000
0.4–0.6	10.0–10.5	1 313 521	0.775 ± 0.000	0.000 ± 0.000	0.741 ± 0.000	0.094 ± 0.000	0.455 ± 0.002	0.194 ± 0.000	0.873 ± 0.001	0.161 ± 0.001	0.761 ± 0.002	0.078 ± 0.001
0.6–0.8	9.0–9.5	4 717 101	0.782 ± 0.000	0.445 ± 0.001	0.539 ± 0.000	0.078 ± 0.000	0.262 ± 0.001	0.189 ± 0.000	0.745 ± 0.001	0.281 ± 0.001	0.667 ± 0.001	0.052 ± 0.000
0.6–0.8	9.5–10.0	3 779 549	0.748 ± 0.000	0.286 ± 0.002	0.619 ± 0.000	0.104 ± 0.000	0.258 ± 0.002	0.205 ± 0.000	0.811 ± 0.001	0.119 ± 0.001	0.727 ± 0.001	0.154 ± 0.001
0.6–0.8	10.0–10.5	1 898 979	0.725 ± 0.000	0.219 ± 0.002	0.725 ± 0.000	0.142 ± 0.000	0.196 ± 0.002	0.208 ± 0.000	0.832 ± 0.001	0.024 ± 0.001	0.701 ± 0.001	0.275 ± 0.001
0.8–1.0	9.0–9.5	4 362 066	0.775 ± 0.000	0.505 ± 0.000	0.541 ± 0.000	0.067 ± 0.000	0.230 ± 0.001	0.172 ± 0.000	0.577 ± 0.001	0.349 ± 0.001	0.605 ± 0.001	0.047 ± 0.000
0.8–1.0	9.5–10.0	4 416 628	0.731 ± 0.000	0.350 ± 0.001	0.617 ± 0.000	0.102 ± 0.000	0.218 ± 0.001	0.194 ± 0.000	0.706 ± 0.001	0.122 ± 0.001	0.676 ± 0.001	0.202 ± 0.001
0.8–1.0	10.0–10.5	2 067 640	0.671 ± 0.000	0.258 ± 0.002	0.716 ± 0.000	0.160 ± 0.000	0.184 ± 0.002	0.207 ± 0.000	0.724 ± 0.001	0.022 ± 0.001	0.540 ± 0.001	0.438 ± 0.001
1.0–1.2	9.0–9.5	1 875 729	0.771 ± 0.000	0.547 ± 0.001	0.525 ± 0.000	0.059 ± 0.000	0.216 ± 0.001	0.161 ± 0.000	0.362 ± 0.003	0.419 ± 0.001	0.544 ± 0.001	0.038 ± 0.000
1.0–1.2	9.5–10.0	2 961 898	0.716 ± 0.000	0.392 ± 0.001	0.600 ± 0.000	0.096 ± 0.000	0.212 ± 0.001	0.185 ± 0.000	0.518 ± 0.001	0.151 ± 0.001	0.608 ± 0.001	0.241 ± 0.001
1.0–1.2	10.0–10.5	1 480 278	0.600 ± 0.001	0.205 ± 0.009	0.692 ± 0.000	0.166 ± 0.000	0.324 ± 0.009	0.200 ± 0.000	0.536 ± 0.002	0.067 ± 0.002	0.335 ± 0.002	0.599 ± 0.001

Appendix G: Visual examples of galaxies by class probability

Following section 3.4 of P24 (also section 5.1 of Z19), we use the posterior means of the model histograms to determine the relative contributions from each 3D ellipsoid class, assigning a class probability to each galaxy based only on observed $\log_{10}(a)$ and b/a values rather than population-level fractions. We then examine *Euclid* VIS image cutouts[1] for 'high-probability' candidates (galaxies with individual class probabilities $> 75\%$, an arbitrary threshold) across various mass-redshift bins. Figure G.1 shows several examples of these cutouts for the prolate (top row), oblate (middle row) and spheroid (bottom row) classes. Visual inspection reveals both consistencies and differences from figure 17 of P24.

Within this sample, only 34 galaxies have $P_{\rm prolate} > 75\%$. The cutouts in the top row of Fig. G.1 show the most common type of cutout seen for prolate candidates. Our high-probability prolate candidates appear more compact, with bright cores and only slightly extended features, making visual shape determination ambiguous. While these example candidates have the highest $P_{\rm prolate}$, they have an angular $R_{\rm e}$ only 1.1–1.4 times the VIS PSF FWHM and are therefore barely resolved, and most lie at $\log_{10}(M_*/M_\odot) > 9.5$, outside the low-mass bins in which the prolate-to-oblate trend is found. The prolate candidates in the top two rows of figure 14 in P24 exhibit clearer extended disc components in false-colour RGB images, though these are at higher redshifts than our sample.

Several galaxies with $P_{\rm oblate} > 75\%$ are shown in the middle row of Fig. G.1. The first four cutouts show oblate candidates that appear to be face-on spiral galaxies, consistent with cutouts from the middle two rows of figure 14 in P24. While most high-probability oblate candidates resemble these, the last two cutouts in the middle row show candidates that appear to be edge-on disc galaxies, in two different mass-redshift bins. As discussed in Sect. 2, prolate and oblate galaxies viewed edge-on are difficult to distinguish, since edge-on discs occupy the same low-b/a region as intrinsically elongated systems. However, both edge-on examples here have very large b/a values and observed sizes larger than the range spanned by the 3D ellipsoid model library ($\log_{10}(a) \in [-1, 1]$, corresponding to $a \sim 0.1$–10 kpc). Thus, the classification is effectively an extrapolation, and the edge-on disc interpretation cannot be reliably distinguished from a genuinely elongated system for these objects on the basis of b/a and $\log_{10}(a)$ alone.

The final row of Fig. G.1 shows examples of high-probability spheroid candidates. These cutouts appear compact, round, and centrally concentrated, with smooth light profiles and no apparent disc components – consistent with those in the bottom two rows of figure 14 in P24. We stress that these are illustrative examples, selected as those with the highest class probabilities computed from observed b/a and $\log_{10}(a)$ values alone. The same two projected parameters that drive our population-level inference cannot uniquely determine an individual galaxy's intrinsic 3D shape (Sect. 5.3), so they should not be interpreted as definitive morphological classifications. Combining *Euclid* VIS and NIR imaging, or additional morphological measures, may refine per-object classifications. We defer such analyses to a future paper.

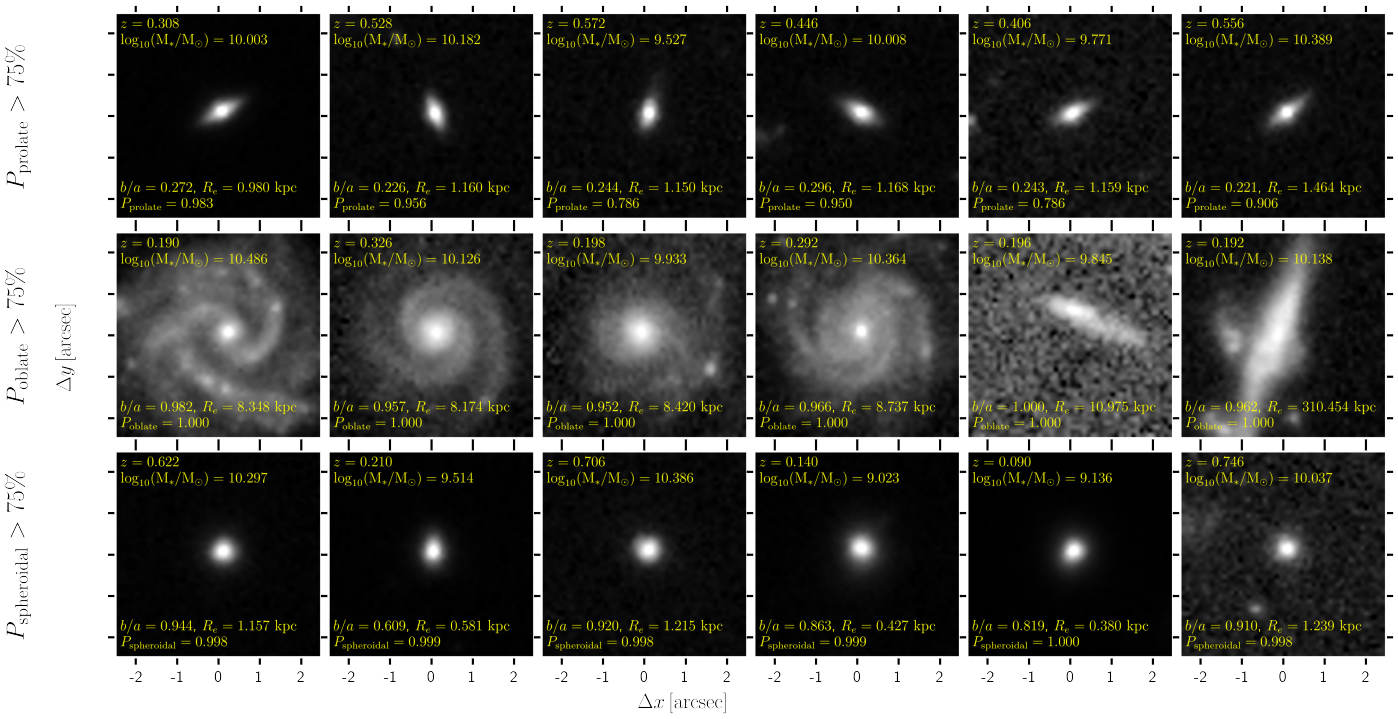


Fig. G.1. Example $5'' \times 5''$ *Euclid* VIS cutouts for prolate (*top*), oblate (*middle*), and spheroid (*bottom*) galaxies with $P_{\rm class} > 75\%$. Each cutout shows the photo-z, stellar mass, Sérsic b/a and $R_{\rm e}$, and class probability. Axes give the offset from the centre of the source in arcseconds.

[1] Cutouts were created using the `Cutana` software (Gómez et al. 2025) on ESA Datalabs (Navarro et al. 2024).

Appendix H: Per-bin observed, model, and residual histograms

Figures H.1–H.18 show, for each mass–redshift bin, the observed and posterior-mean model b/a–$\log_{10}(a)$ histograms, together with the residuals $N_{\rm obs} - N_{\rm model}$ and the Pearson residuals $(N_{\rm obs} - N_{\rm model})/\sqrt{N_{\rm model}}$, computed over the cells used in the likelihood. The residuals indicate systematic differences between the data and the single trivariate Gaussian model that are not captured by the statistical uncertainties in Table F.2.

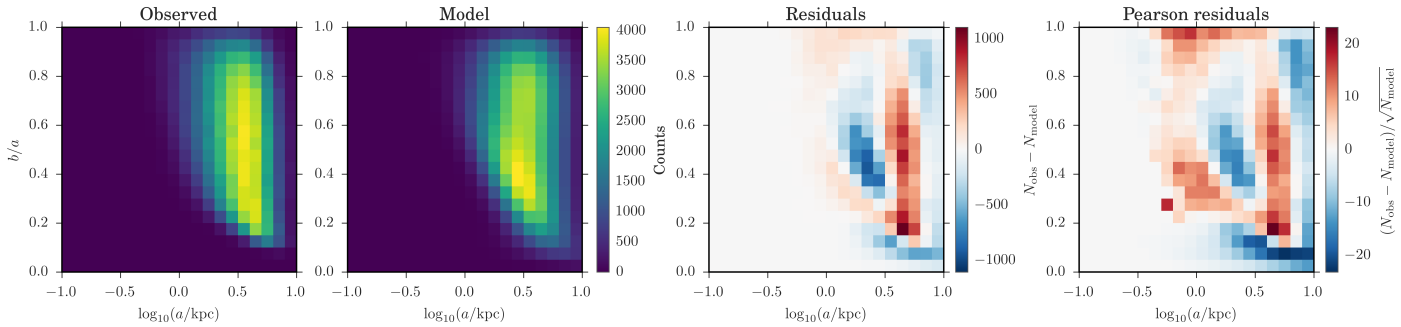


Fig. H.1. Observed (first panel) and posterior-mean model (second panel) b/a–$\log_{10}(a)$ histograms for the $0.0 < z < 0.2$, $9.0 < \log_{10}(M_*/M_\odot) < 9.5$ bin, with the residuals $N_{\rm obs} - N_{\rm model}$ (third panel) and the Pearson residuals $(N_{\rm obs} - N_{\rm model})/\sqrt{N_{\rm model}}$ (fourth panel). Colour bars give galaxy counts for the histograms, the difference in counts for the residuals, and the dimensionless Pearson residual for the last panel.

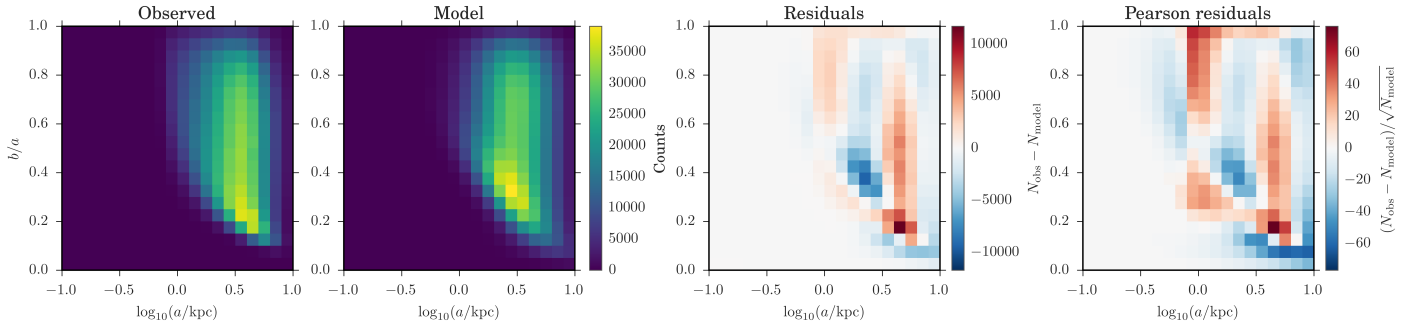


Fig. H.2. Same as Fig. H.1, but for the $0.2 < z < 0.4$, $9.0 < \log_{10}(M_*/M_\odot) < 9.5$ bin.

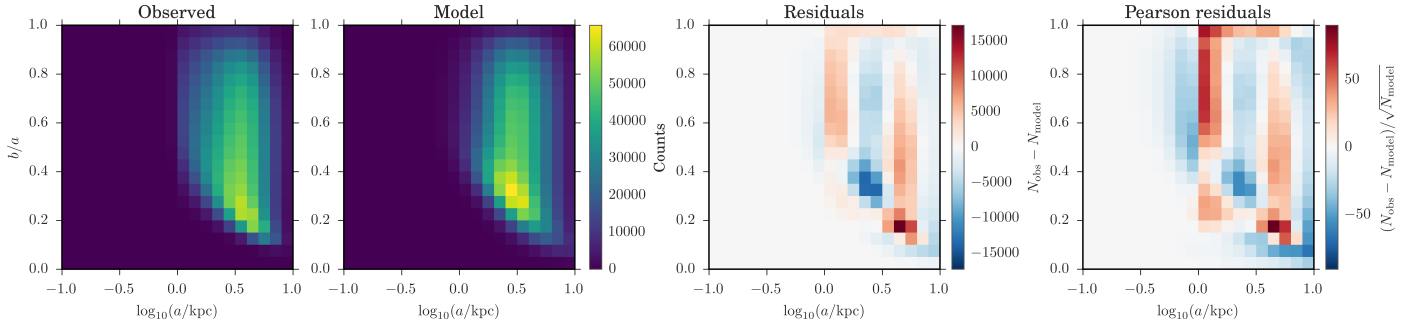


Fig. H.3. Same as Fig. H.1, but for the $0.4 < z < 0.6$, $9.0 < \log_{10}(M_*/M_\odot) < 9.5$ bin.

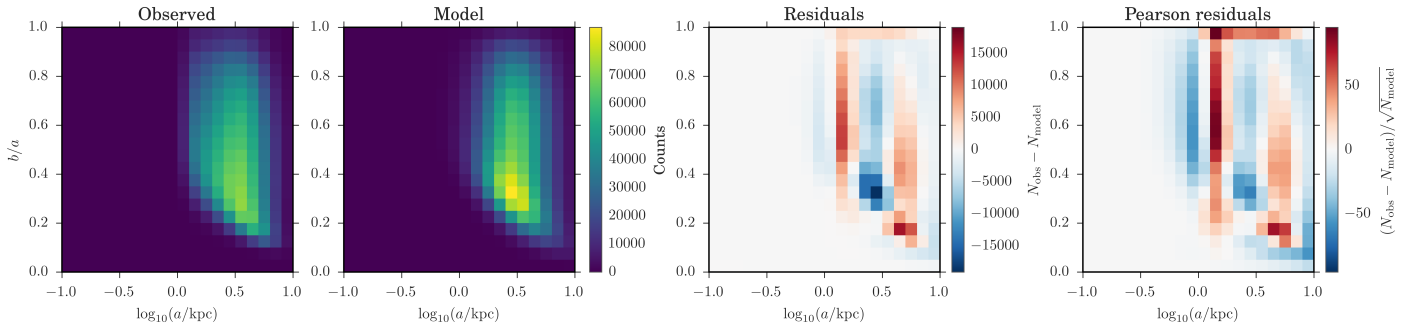


Fig. H.4. Same as Fig. H.1, but for the $0.6 < z < 0.8$, $9.0 < \log_{10}(M_*/M_\odot) < 9.5$ bin.

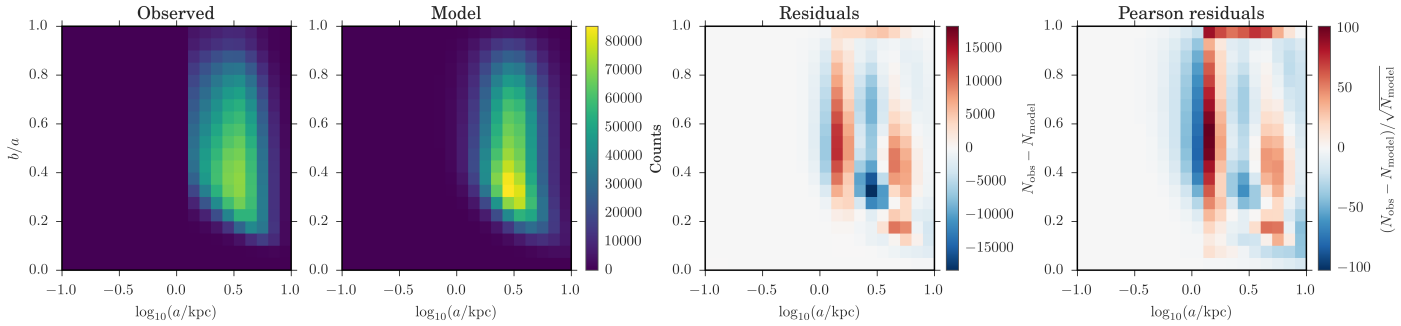


Fig. H.5. Same as Fig. H.1, but for the $0.8 < z < 1.0$, $9.0 < \log_{10}(M_*/M_\odot) < 9.5$ bin.

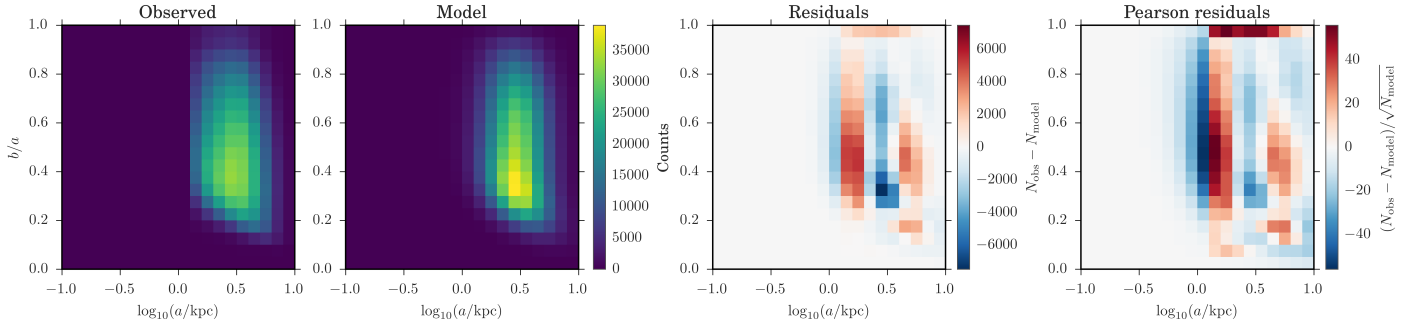


Fig. H.6. Same as Fig. H.1, but for the $1.0 < z < 1.2$, $9.0 < \log_{10}(M_*/M_\odot) < 9.5$ bin.

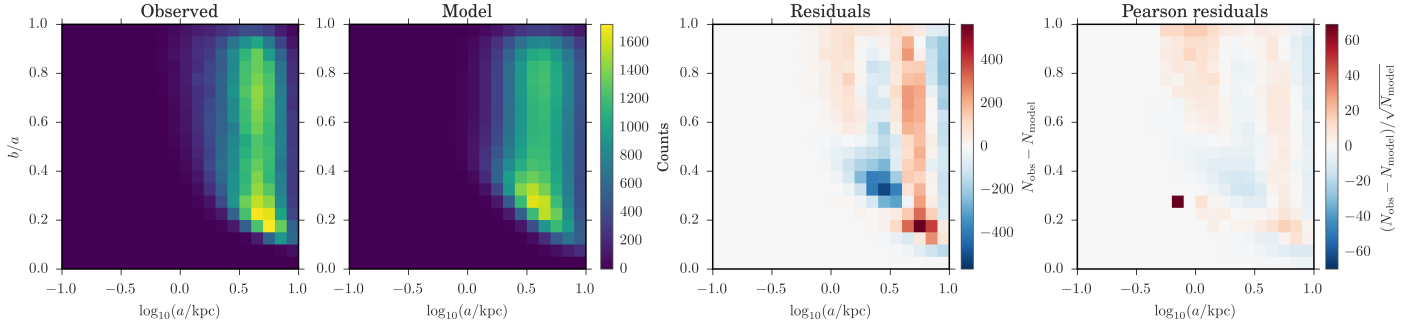


Fig. H.7. Same as Fig. H.1, but for the $0.0 < z < 0.2$, $9.5 < \log_{10}(M_*/M_\odot) < 10.0$ bin.

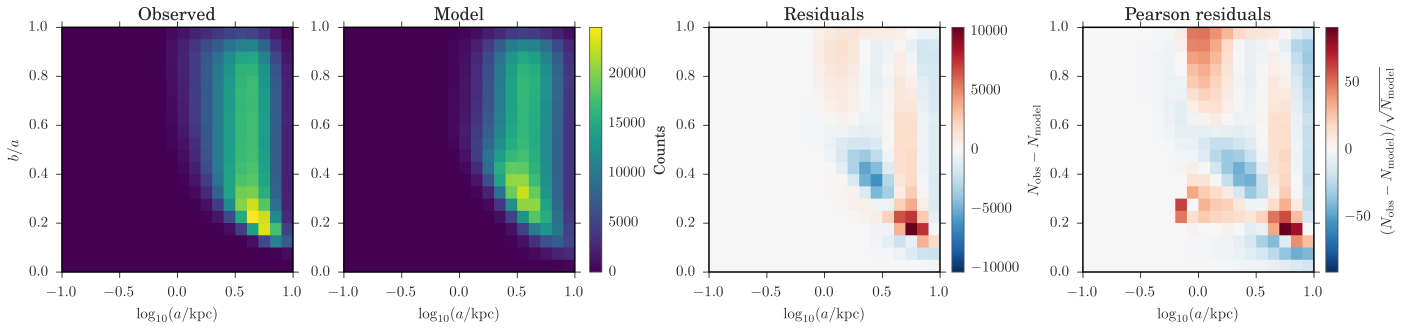


Fig. H.8. Same as Fig. H.1, but for the $0.2 < z < 0.4$, $9.5 < \log_{10}(M_*/M_\odot) < 10.0$ bin.

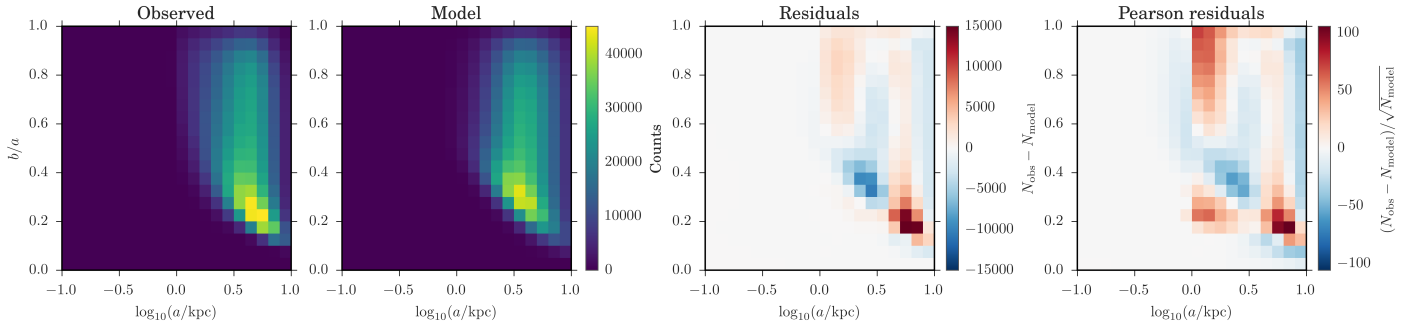


Fig. H.9. Same as Fig. H.1, but for the $0.4 < z < 0.6$, $9.5 < \log_{10}(M_*/M_\odot) < 10.0$ bin.

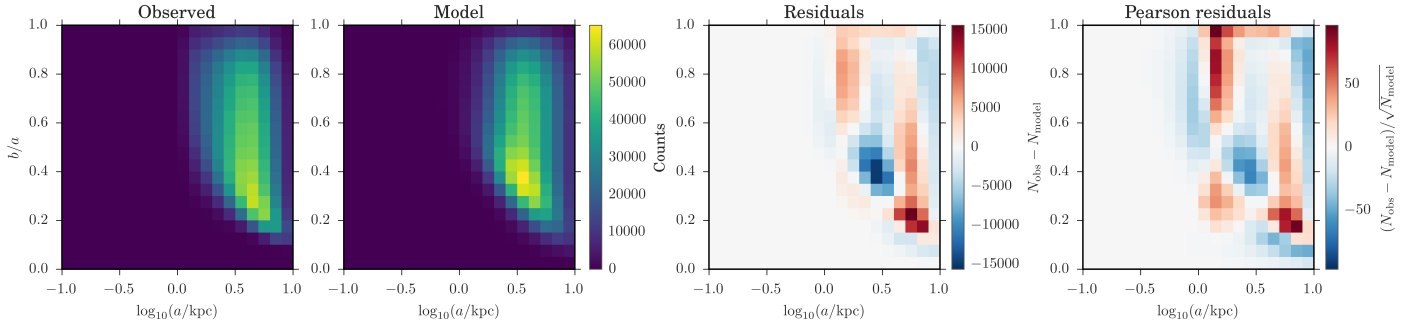


Fig. H.10. Same as Fig. H.1, but for the $0.6 < z < 0.8$, $9.5 < \log_{10}(M_*/M_\odot) < 10.0$ bin.

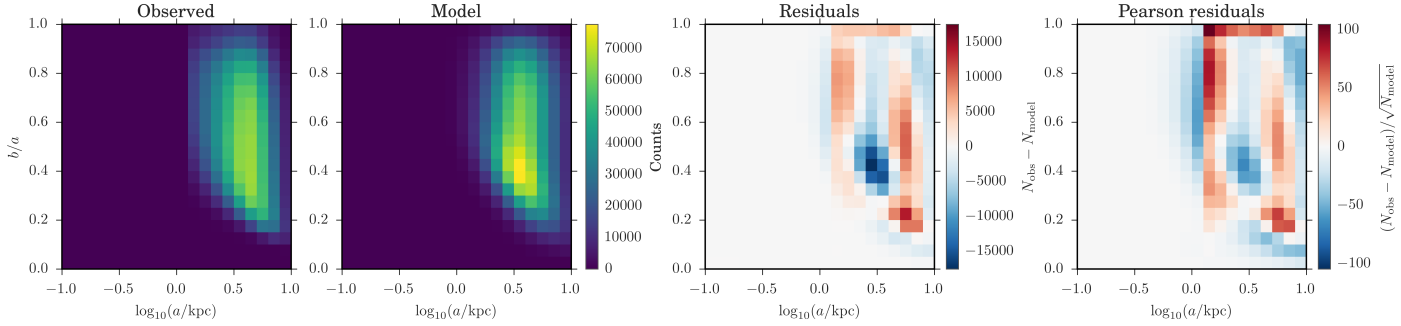


Fig. H.11. Same as Fig. H.1, but for the $0.8 < z < 1.0$, $9.5 < \log_{10}(M_*/M_\odot) < 10.0$ bin.

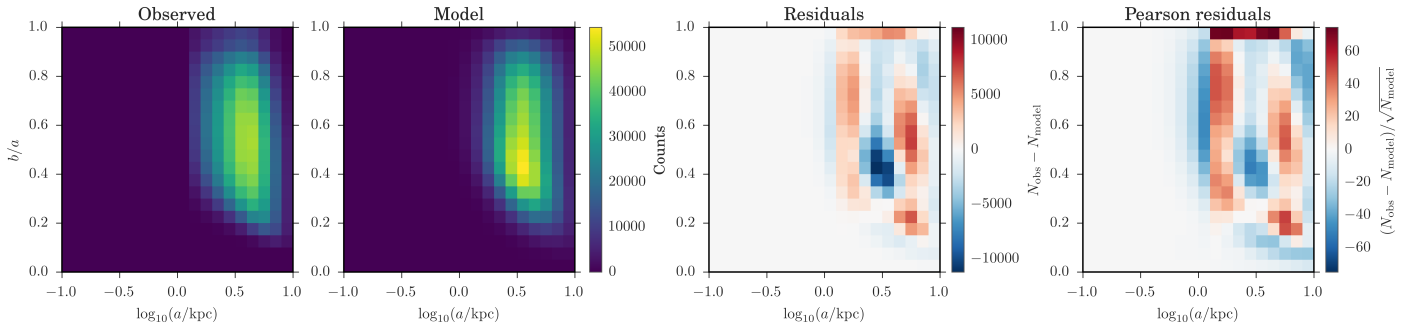


Fig. H.12. Same as Fig. H.1, but for the $1.0 < z < 1.2$, $9.5 < \log_{10}(M_*/M_\odot) < 10.0$ bin.

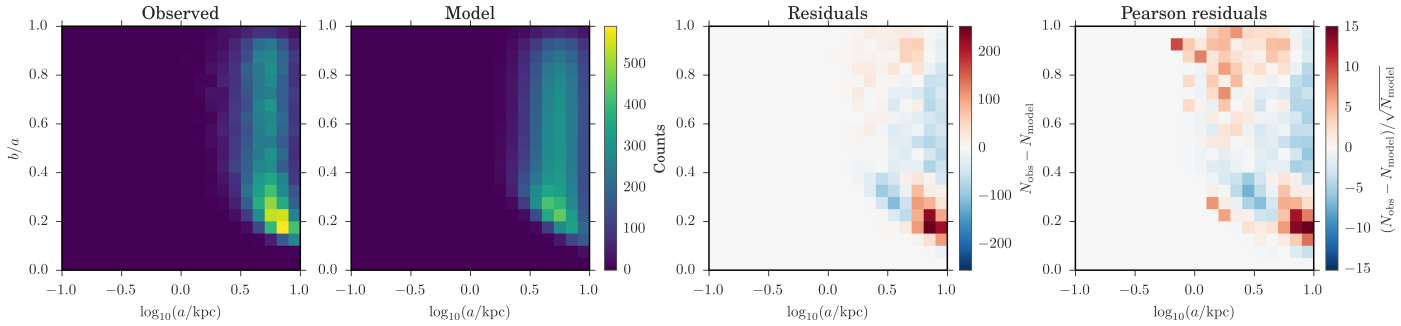


Fig. H.13. Same as Fig. H.1, but for the $0.0 < z < 0.2$, $10.0 < \log_{10}(M_*/M_\odot) < 10.5$ bin.

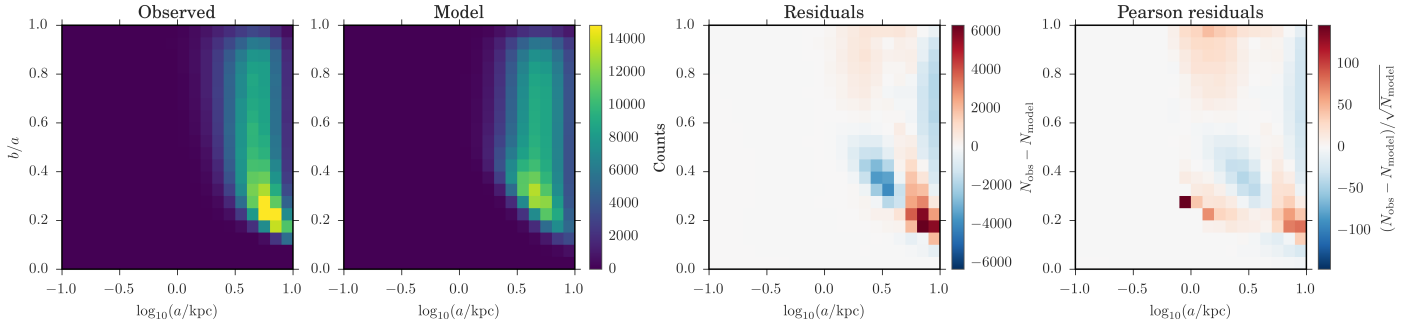


Fig. H.14. Same as Fig. H.1, but for the $0.2 < z < 0.4$, $10.0 < \log_{10}(M_*/M_\odot) < 10.5$ bin.

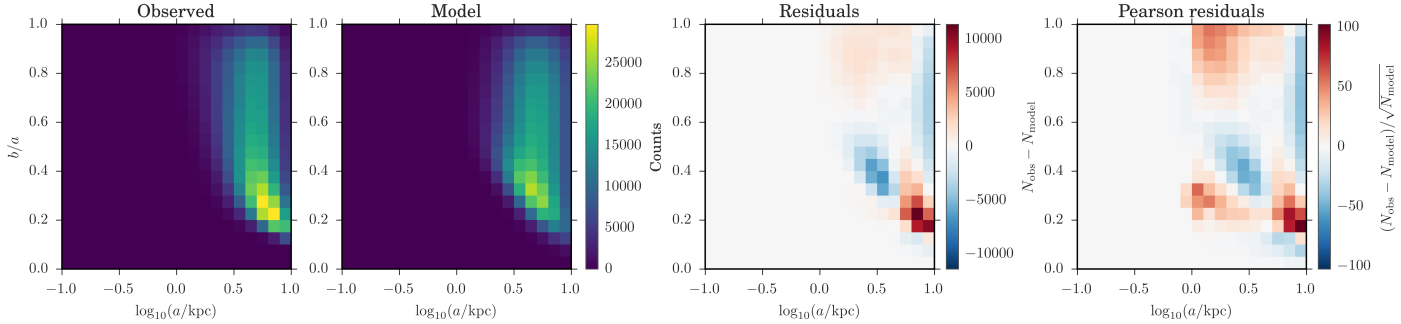


Fig. H.15. Same as Fig. H.1, but for the $0.4 < z < 0.6$, $10.0 < \log_{10}(M_*/M_\odot) < 10.5$ bin.

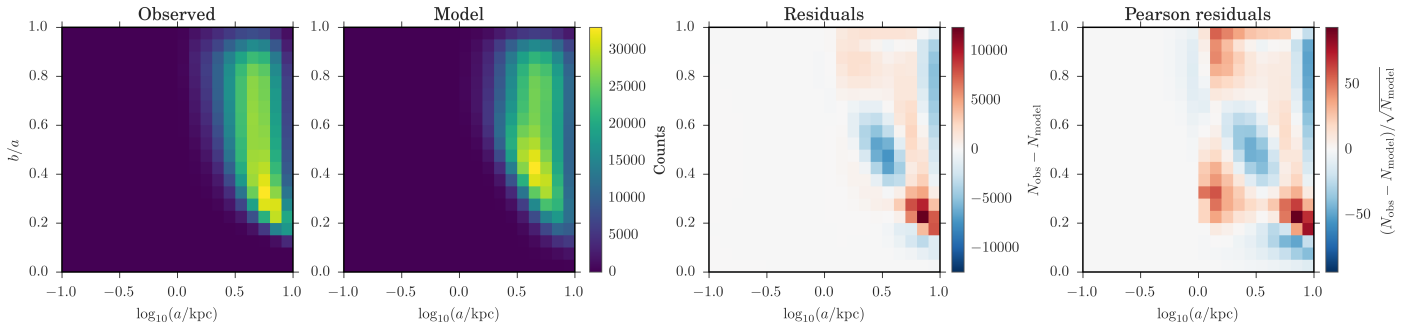


Fig. H.16. Same as Fig. H.1, but for the $0.6 < z < 0.8$, $10.0 < \log_{10}(M_*/M_\odot) < 10.5$ bin.

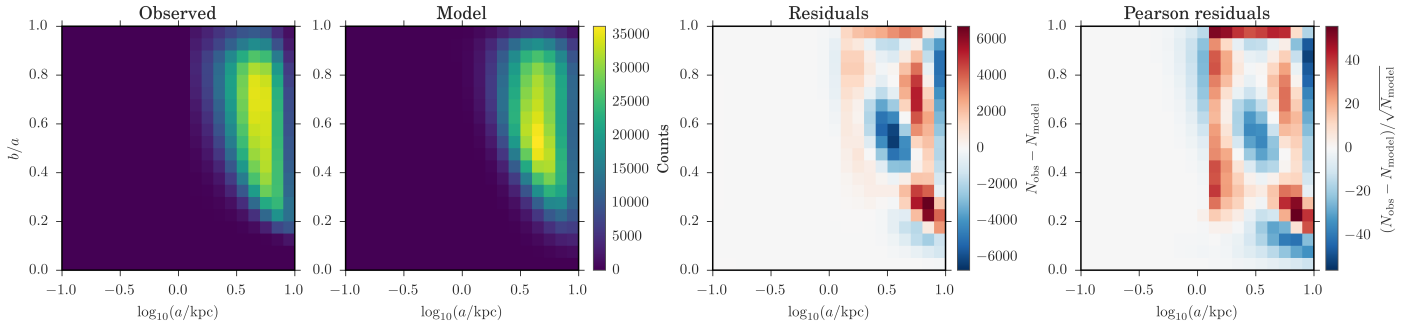


Fig. H.17. Same as Fig. H.1, but for the $0.8 < z < 1.0$, $10.0 < \log_{10}(M_*/M_\odot) < 10.5$ bin.

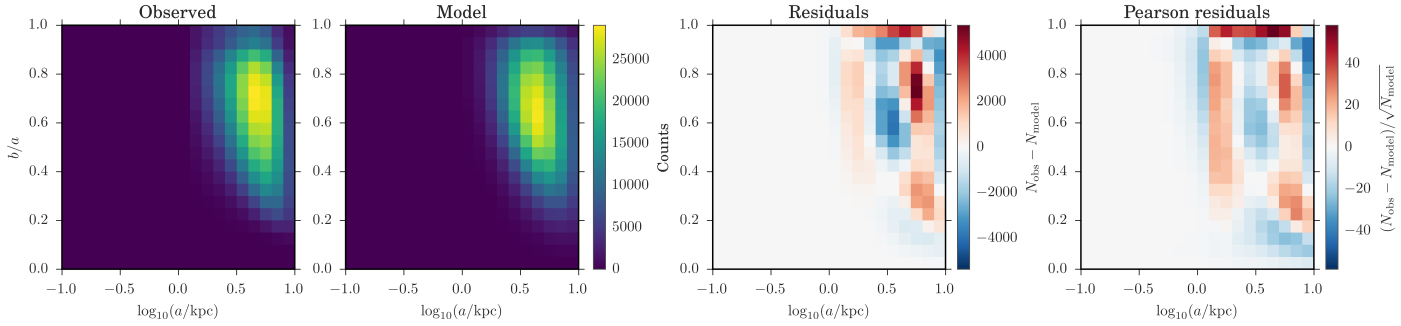


Fig. H.18. Same as Fig. H.1, but for the $1.0 < z < 1.2$, $10.0 < \log_{10}(M_*/M_\odot) < 10.5$ bin.